JGR Solid Earth

RESEARCH ARTICLE
10.1029/2020JB020652

Thermal Weakening Friction During Seismic Slip: Experiments and Models With Heat Sources and Sinks

S. Nielsen[1], E. Spagnuolo[2], M. Violay[3], and G. Di Toro[4]

[1]Department of Earth Sciences, Durham University, Durham, UK, [2]Sismologia e Tettonofisica, Istituto Nazionale di Geofisica e Vulcanologia, Rome, Italy, [3]Faculté de l'Environnement Naturel, Architectural et Construit (ENAC), Laboratory of Experimental Rock Mechanics (LEMR), École Polytechnique Fédérale de Lausanne (EPFL), Lausanne, Switzerland, [4]Dipartimento di Geoscienze, Università degli Studi di Padova, Padova, Italy

Key Points:

- Thermal dependence of diffusivity and heat capacity can have a large effect on temperature and friction during co-seismic slip
- The effects of thermal dependence on friction can be approximately emulated in a model with constant parameters by tuning the energy sinks
- We compare the efficiency of three different numerical solutions (Finite differences, wavenumber summation, and integral solution

Supporting Information:

Supporting Information may be found in the online version of this article.

Correspondence to:

S. Nielsen,
stefan.nielsen@durham.ac.uk

Citation:

Nielsen, S., Spagnuolo, E., Violay, M., & Di Toro, G. (2021). Thermal weakening friction during seismic slip: Experiments and models with heat sources and sinks. *Journal of Geophysical Research: Solid Earth*, *126*, e2020JB020652. https://doi.org/10.1029/2020JB020652

Received 24 JUL 2020
Accepted 29 MAR 2021

Abstract Experiments that systematically explore rock friction under crustal earthquake conditions reveal that faults undergo abrupt dynamic weakening. Processes related to heating and weakening of fault surfaces have been invoked to explain pronounced velocity weakening. Both contact asperity temperature T_a and background temperature T of the slip zone evolve significantly during high-velocity slip due to heat sources (frictional work), heat sinks (e.g., latent heat of decomposition processes), and diffusion. Using carefully calibrated High-Velocity Rotary Friction experiments, we test the compatibility of thermal weakening models: (1) a model of friction based only on T in an extremely simplified, Arrhenius-like thermal dependence; (2) a flash heating model which accounts for the evolution of both V and T; (3) same but including heat sinks in the thermal balance; and (4) same but including the thermal dependence of diffusivity and heat capacity. All models reflect the experimental results but model (1) results in unrealistically low temperatures and model (2) reproduces the restrengthening phase only by modifying the parameters for each experimental condition. The presence of dissipative heat sinks in stage (3) significantly affects T and reflects on the friction, allowing a better joint fit of the initial weakening and final strength recovery across a range of experiments. Temperature is significantly altered by thermal dependence of (4). However, similar results can be obtained by (3) and (4) by adjusting the energy sinks. To compute temperature in this type of problem, we compare the efficiency of three different numerical approximations (finite difference, wavenumber summation, and discrete integral).

Plain Language Summary During earthquakes, fast slip on the fault generates large amounts of localized heat. The consequent temperature rise has been proposed as one main cause of abrupt frictional weakening, concomitant with decomposition reactions, which act as heat sinks, partially buffering the temperature rise. Here we test models of thermal weakening by computing the temperature evolution and the temperature-dependent friction, showing the importance of accounting for heat sources, heat sinks, and local variation of rock properties due to rising temperatures.

1. Introduction

Well-studied Dieterich-Ruina rate-and-state laws (Dieterich, 1979; Marone, 1998; Ruina, 1983) describe accurately the friction under slow, aseismic creep. However, it has been long recognized in models of earthquake rupture that it is necessary to account for the presence of more radical dynamic weakening at high slip velocity. In a few cases, it has been possible to constrain some aspects of co-seismic sliding friction: the absolute stress level was obtained using rake rotation of slip during the Kobe, 1995 earthquake (Spudich, 1998), or the rotation of focal mechanisms in small earthquakes before and after the main rupture of Tohoku, 2011 earthquake (Hardebeck, 2015; Hasegawa et al., 2011); both cases indicated that the sliding friction must have been extremely low. In addition, a very low temperature increase was measured months after the Tohoku earthquake in a borehole across the fault, again compatible with low co-seismic sliding friction (Fulton et al., 2013). Finally, the weakening distance for several earthquakes was estimated from seismological data. Using strong-motion records containing Mach waves from the Denali, 2002 and the Izmit, 1999 earthquakes Cruz-Atienza and Olsen (2010) estimated a distance ≈ 1.5–1.7. For the Kaikōura, 2016 earthquake estimates of several meters were obtained by Kaneko et al. (2017). Also for ,Kaikōura Ulrich et al. (2019) used dynamic rupture numerical simulations to obtain two different estimates. The first one analyzing the frictional slip-stress curves indicated distances of 0.2–0.5 m, the second one, obtained by

analyzing the synthetic seismograms, resulted in estimates of several meters. However, as noted by Ulrich et al. (2019), the second estimate is expected to yield larger values because it implicitly includes the effects of off-fault damage in the rupture energy budget (Nielsen, Spagnuolo, Smith, et al., 2016). In spite of such rare highlights, dynamic weakening remains difficult to quantify based on seismological earthquake data. Hence, a number of laws with enhanced velocity-weakening have been implemented in models of seismic fault rupture (Nielsen & Madariaga, 2003; Noda et al., 2009; Zheng & Rice, 1998), relying mostly on theoretical arguments (Archard, 1959; Beeler et al., 2008; Nielsen et al., 2008; Noda et al., 2009; Rempel & Rice, 2006; Rempel & Weaver, 2008; J. R. Rice, 2006, and references therein).

On the other hand, an increasing number of well-constrained observations are being obtained in laboratory experiments performed under close to co-seismic conditions. Yuan and Prakash (2008, 2012) used an impact bar to load impulsively a frictional slip surface under extreme conditions of slip rate (tens of meters per second) and normal stress (hundreds of Mega Pascals) while measuring the shear resistance to slip; they found an abrupt weakening occurring over extremely short slip distances (<1 μm) and times (<1 μs). Intermediate, more seismic-like conditions were studied (0.5–6.5 m/s, 1–50 MPa) using rotary shear machines (Di Toro et al., 2004, 2006; Fondriest et al., 2013; Han et al., 2007; Hirose & Shimamoto, 2005; Mizoguchi et al., 2007; Sone & Shimamoto, 2009; Tsutsumi & Shimamoto, 1997; Violay, Nielsen, Gibert et al., 2013; Violay et al., 2015) also resulting in pronounced weakening; however, in the latter experiments, the measured weakening distances were much longer (of the order of tens of centimeters to several meters).

In the case of frictional melting, the role of temperature and frictional power in the weakening was directly modeled, and it was shown that the weakening was accelerated under larger normal stress and slip velocity (Nielsen, Mosca, et al., 2010). Theoretical arguments (Nielsen et al., 2008) predicted that the final, steady-state friction level depended on normal stress to a power 1/4, which was later confirmed by accurate experiments (Violay et al., 2014). The center of the molten layer can reach peak temperatures well above those of melting temperatures of the rock-constituent minerals (overheating), creating an ultra-thin, ultra-low viscosity slip layer whose lubricant effect is all the more efficient when slip rate and normal stress are elevated. However previous modeling of frictional melt during the transient weakening (Nielsen, Mosca, et al., 2010) relies on a complex, explicit numerical model; in addition, the model considers cases where melting is observed (in silica-built rocks) but not the cases where no melting occurs—for example, carbonate rocks (Han et al., 2007; Violay, Nielsen, Spagnuolo et al., 2013)—although, there too, considerable weakening takes place. Thermal pressurization of fluids confined to a narrow fault zone has also been invoked as a cause for profound weakening in natural faults (Rempel & Rice, 2006; J. R. Rice, 2006). Such mechanism may take place in fluid-saturated, relatively low permeability fault zones, and modeling shows that it can be compatible with the estimates of fracture energy from natural earthquakes (J. R. Rice, 2006; Viesca & Garagash, 2015). In a few cases, high-velocity experiments were conducted with fluids under drained and undrained conditions, on bare rock samples with no gouge, showing the onset of thermal pressurization only in the later phases of the slip where friction was already low(Violay et al., 2011, 2015; Violay, Nielsen, Gibert et al., 2013; Violay, Nielsen, Spagnuolo et al., 2013). However, it is observed in most high-velocity friction experiments that extremely fast, efficient weakening takes place on natural rocks even in the absence of fluids.

Drawing on early studies of flash heating of asperities in metal friction (Archard, 1959), Rice (J. Rice, 1999; J. R. Rice, 2006) introduced a model for rock friction at high slip rates where temperature rise is implicit and the asperities weakening is essentially related to slip velocity; such flash-weakening model was subsequently discussed by Beeler et al. (2008) and Rempel and Weaver (2008). These works were followed by a rapidly developing body of studies on thermal weakening during fast slip, from either experimental tests on specific lithologies—for example, serpentine (Proctor et al., 2014), illite and quartz gouge (Yao et al., 2016)—or theoretical modeling perspectives—for example, thermal pressurization (Brantut & Platt, 2017) and flash weakening (Brantut & Viesca, 2017).

It has been claimed that slip acceleration (Chang et al., 2012) plays a fundamental role in dynamic friction reduction; however, combined high slip velocity and high normal stress, producing high frictional power, appear to be the key requirements to induce pronounced weakening (Di Toro et al., 2011) independently of the imposed acceleration. In fact one direct consequence of elevated frictional power is to induce an elevated and localized temperature growth on the slip surface and its immediate vicinity; accordingly high

temperature has been indicated as a likely cause of dynamic frictional weakening. On the other hand, the direct effect of temperature on the weakening may be questioned. Experiments conducted on preheated samples of dolerite (Noda et al., 2011) with the use of a furnace, and on Westerly granite, India gabbro, and quartzite (Noda et al., 2011; Passelègue et al., 2014), reveal a correlation between weakening and temperature, independently of slip velocity, although the weakening is relatively modest. Frictional weakening of pre-heated olivine samples at slow slip rates is even more modest (King & Marone, 2012). We shall discuss these results here in terms of localized versus background temperature changes.

Here, we discuss aspects of frictional contact and the effects of heating under high-velocity sliding. We define a model based on the flash-weakening formalism discussed above (Archard, 1959; Beeler et al., 2008; Rempel & Weaver, 2008; J. Rice, 1999; J. R. Rice, 2006), and extend it to include the effect of frictional heating on the background temperature, thermal diffusion, and the presence of heat sinks due to decomposition or melting. We propose an extension to account for the onset of frictional melting and shortening. We indicate a parsimonious numerical scheme for the temperature update. Assumptions and approximations are used to obtain a sufficiently elementary and uncomplicated model for practical use as a friction law in earthquake slip models, while retaining the essential behavior observed during rock test experiments under coseismic conditions.

Temperature evolution is important in the weakening behavior, but its accurate numerical evaluation can be costly and inefficient over an extended number of time steps. Such cost may become prohibitive when the temperature needs to be evaluated at many different points in an extended fault model. Here we test three different temperature computation schemes and compare the efficiency and the flexibility of each (see Appendix A). First, the temperature resulting from an imposed boundary flow can be written as an analytical integral, which can be directly discretized and solved numerically. This is easy to implement, but by far the least efficient approach, and it does not allow to include variations of the parameters in time or in space. Second, a spatial Fourier transform of the diffusion equation can be written, and a discrete wavenumber equation (Noda & Lapusta, 2010) can be solved numerically. Accuracy within a few percent can be achieved with a small number of memory variables (16 or less) which are updated at each iteration and can be augmented to an arbitrary level by increasing the number of memory variables. The scheme is easily implemented and can be integrated with existing numerical codes. It is far more efficient than the direct summation, but in this method, too, it is not easy to include parameter variability in time and space. Finally, we implement the classic finite difference method with a Crank-Nicolson scheme, where variables are defined on a grid of nodes in space and time. In conditions of frictional heating, this method to solve for temperature diffusion is the most flexible, and—from our tests in either Python 3.7 or Fortran 90 on a desktop computer—it can achieve equal accuracy in less time than the two other methods, if correctly configured. However, it is slightly more costly in terms of memory than the wavenumber method. In addition, it allows to include a moving boundary to solve the Stefan problem (Carslaw & Jaeger, 1959; Nielsen, Mosca, et al., 2010) in the presence of melting, and allowing to introduce spatial and time variations in the parameters, as illustrated in Section 6.

The models are calibrated and tested against a number of selected rotary shear, high-velocity experiments performed on the SHIVA machine hosted at Istituto Nazionale di Geofisica e Vulcanologia, Roma. We used hollow cylindrical samples of 30/50 mm inner/outer diameter, respectively, machined from gabbro (as a representative of silicate-built rocks) and Carrara marble (as a representative of carbonate-built rocks). The experimental conditions cover the range from 10 to 30 MPa in normal stress and from 1 to 6.5 m/s in slip velocity.

2. Heat Sources and Sinks

The frictional work released per unit time (power) per unit area on the sliding interface is

$$q_f = \tau(t)\, V(t) \tag{1}$$

where V is the slip rate and τ is a macroscopic average of the shear stress. Frictional work is responsible for temperature rise, but it is in part dissipated by thermal diffusion and in part by other endothermal processes (latent heat for melting, decomposition, heat removal by fluid mass escape from the interface, surface

energy involved in comminution, etc.). The latter processes are known to act as a buffer which inhibits the continuous rise of temperature; we argue that they have a significant effect on the background temperature and friction.

Assuming that the frictional heat rate from Equation 1 takes place on the fault surface (or within a principal slip zone of negligible thickness) at $z = 0$ and propagates away from the fault surface, we may write the one-dimensional thermal diffusion equation

$$\partial_t T = \kappa \partial_z^2 T + \frac{\delta(z)\, q}{\rho\, c} \tag{2}$$

where $\delta(z)$ is the Dirac delta function, ρ is the mass density, c is the heat capacity and κ is the thermal diffusivity. The net heat source q can be described as the difference between frictional heating q_f and the sinks q_s:

$$q(t) = 1/2\Big[\tau(t)\, V(t) - q_s\big(T(t)\big)\Big] \tag{3}$$

where the 1/2 factor indicates that the available heat will propagate on both sides of the fault. Finally, the shear stress τ arises from the sliding friction, which is arguably a function of sliding rate V, temperature T, and any number of state variables:

$$\tau(t) = f(V, T, \ldots) \tag{4}$$

We delay to Section 5 the discussion of particular forms of Equation 4 including thermal dependence, and their compatibility with observed experiments of high velocity friction, and discuss here the nature of possible heat sinks.

The temperature-limiting effect of thermal decomposition has been modeled explicitly in the case of carbonate rocks (Sulem & Famin, 2009), gypsum (Brantut et al., 2010), and dolomite with application to the emplacement of a giant landslide (Mitchell et al., 2015). Generally, the kinetics of a reaction is accelerated exponentially with temperature (Arrhenius kinetics), as a consequence the rate of latent heat loss should increase likewise. In the case of experiments performed in the open air or in a water-filled vessel, there is an additional heat loss (Newton's law of cooling, generally considered as proportional to the temperature difference between a body and the surrounding fluid), which is enhanced by the presence of fluid convection (Acosta et al., 2018; Violay, Nielsen, Gibert, et al., 2013).

On the other hand, if the thermal dependence of diffusivity and heat capacity is considered, an increase in temperature can result in a decrease in thermal conductivity (Merriman et al., 2018). This will increase the insulating property of the rock (at least locally in the rock layer where temperature rise is substantive) inducing a feedback that enhances the temperature rise. This effect can then counteract the action of the heat sinks. This competition between the two mechanisms is further investigated in Section 6.

Heat loss due to a constant flow rate of cooling fluid may be approximated as $q_s = \psi\,(T - T_i)$ per unit time, assuming that fluid enters the interface at T_i (ambient rock temperature) and exits at temperature T (background interface temperature); ψ is the heat capacity of the fluid times its flow rate (per unit area).

Heat loss due to decomposition processes will be represented by an exponential Arrhenius law of the form (Sulem & Famin, 2009):

$$q_s = \alpha\,(1-n)\,h\,\rho\,L\,A\,\exp\left(-\frac{E_a}{R\,T}\right) \tag{5}$$

Here h is the thickness of the zone affected by the decomposition, $(1 - n)$ is the remaining proportion of (unreacted) material (in first approximation $1 - n \approx 1$), and $R = 8.31\mathrm{JK}^{-1}\,\mathrm{mol}^{-1}$. Note that in Equation 5 T is the absolute temperature, but in the following sections T is the excess above initial temperature. In the example of decarbonation of pure calcite, indicative literature values (Sulem & Famin, 2009) are $E_a = 319\ 10^3$ J/mol, $A = 2.95\ 10^{15}\ \mathrm{s}^{-1}$, $L = 3190\ 10^3$ J/kg, for activation energy, pre-exponential factor and latent heat,

respectively, $\rho = 3{,}000$ kg m^{-3} and $R = 8.31$. Defining $C_s = (1 - n)\, h\, \rho\, L\, A$ and $T_s = E_a/R$, we may re/write the heat loss as

$$q_s = C_s \exp\left(T_s / (T + T_i)\right) \tag{6}$$

We note that the term $q_s(T(t))$ in Equation 3 implicitly describes heat sinks that are distributed over a finite thickness h. Distributed heat sinks can be explicitly included using the values of temperature and temperature gradient away from the sliding surface which are derived in Equations A14–A15. However here for simplicity, we will assume that the temperature over h can be equated to that of the sliding surface $T = T(z = 0)$ and that h is the constant; a similar approximation was also used in Mitchell et al. (2015).

In the case of frictional melt, the latent heat and melt extrusion have been taken into account explicitly to model temperature evolution and to describe frictional behavior in both steady-state (Nielsen et al., 2008) and transient conditions (Nielsen, Mosca, et al., 2010). In the case of pervasive melting, it is necessary to solve the Stefan problem with an added term of mass transport in Equation 2, a case also discussed further in Section 6.1 and in Appendix B.

3. Nature of the Frictional Interface

3.1. Real and Nominal Contact Area

Shear and normal stress across the sliding interface are supported by local asperities whose real contact area A_r represents only a small fraction α of the nominal area A_n. During slip, asperity contacts coalesce, deform and disappear forming a distribution at various stages of evolution and under continuous renewal. Because rock constitutive minerals yield under a few percent of strain, within each asperity the shear stress reaches the yield point early during its contact lifetime.

After yielding each asperity deforms under either brittle failure or creep, possibly at a very high strain rate; however, it cannot support a stress value much in excess of the yield value, lest yielding would propagate from the asperity into the supporting substrate thus keeping the stress value bounded. Hence, the majority of asperities are close to the yield shear stress τ_y which can be considered as an average asperity value. The bulk frictional force resisting slip can be written as $F = A_r\, \tau_y$ which, normalized by A_n, yields the bulk frictional stress:

$$\tau = \alpha\, \tau_y. \tag{7}$$

α results from the ratio of applied normal stress σ_n to indentation hardness σ_c (or penetration hardness according to Persson, 2000, Chapter 5.1) such that

$$\alpha = \sigma_n / \sigma_c \tag{8}$$

but in any case $\alpha \leq 1$ so that we may write $\alpha = \text{Min}(1, \sigma_n/\sigma_c)$.

We remark that both indentation hardness (Atkins & Tabor, 1965; Hirth & Kohlstedt, 2004; King & Marone, 2012) and yield shear stress (Raterron et al., 2004; Weidner et al., 1994) are observed to have a strong negative temperature dependence. Accordingly, an increasing temperature induces a decrease in τ_y but an increase in α—see also discussion in (Hirth & Beeler, 2015, and references therein). An increase in the area of asperity contact has been documented, for example, in olivine under slow slip velocity (King & Marone, 2012). Since the thermal weakening and contact area increase have antagonistic effects, the temperature dependence of bulk friction τ is not trivial to predict. In fact experiments performed under slow slip velocity do not show a systematic or pronounced frictional drop with temperature (King & Marone, 2012; Noda et al., 2009).

However, under high slip velocity, a pronounced weakening is observed in correspondence of the temperature rise at the interface. First, we shall propose how to reconcile these two conflicting observations based on the role of slip velocity and temperature localization. Then, we shall proceed to the computation of the bulk frictional resistance of the interface based on local, temperature-dependent rheology.

In case that a pervasive lubricant layer develops and fills continuously the space between the asperity contacts (e.g., a pervasive melt layer Nielsen et al., 2010) and supports the bulk of shear and normal stress, the temperature effect on α is buffered as we may consider $\alpha \approx 1$. At this point, $\tau_y = \tau$ is the viscous shear stress supported by the lubricant layer within a principal slip zone (PSZ), and resistance to sliding is due to the viscous shear of a thin melt layer. Though the heating is not localized at the asperity contacts, it is still localized and concentrated within a thin shear layer provided that slip is brief enough (earthquake-like duration, typically seconds) that heat diffusion away from the PSZ is reduced (close to adiabatic conditions). In a different context (no melting), Cornelio et al. (2019, 2020) have shown how viscous fluids permeating natural rock samples affect frictional weakening at high slip velocity by activating elastohydrodynamic lubrication.

3.2. Shear Thickness and Shear Rate

Observations on paleoseismic faults which were active at epicentral depths (≈10 km Di Toro et al., 2005) show that slip often localizes within a PSZ of a limited thickness (of the order of 100 μm or less). Active or fossil faults at moderate depths also often exhibit localized principal slip zones within a wider fault core (De Paola et al., 2008; Collettini et al., 2011; Otsuki et al., 2003; J. R. Rice, 2006; Sibson, 2003 and references therein).

Finally, laboratory experiments conducted under high stress and velocity also report the development of extremely thin PSZs either between two consolidated rock samples or within simulated or natural fault gouge. In the latter case, localization is achieved only after a critical slip of several centimeters (Pozzi et al., 2019, 2018; Smith et al., 2015). The strain rate can be equated either to the ratio of slip velocity to the thickness of the PSZ, in the presence of a pervasive lubricant layer, or in the absence thereof, to the ratio of the slip velocity to asperity height (typically ≈ 10–100 μm).

Since average seismic fault slip velocity estimated during earthquakes is typically $V \approx 1$ m/s, the resulting shear strain rate within the PSZ or within the asperity contacts is extremely high ($\dot{\varepsilon} = V / 10^{-4} = 10^4$ s^{-1}) and is associated with a number of thermally triggered decomposition, alteration or amorphization processes (dehydration, melting, decarbonation, stress corrosion, comminution, etc.) which may directly or indirectly affect friction through the action of pressurization and/or the formation of a lubricant layer (Hirose & Shimamoto, 2005).

The consequence of such extreme localization of strain rate is that a very low equivalent viscosity should be achieved within the PSZ to result in the observed low value of shear stress during fast sliding. In addition, if the shear heating is generated within a very small thickness $h \ll 4\sqrt{\kappa\, t}$ (where t is the duration of the slip, indicatively 1 s), the temperature evolution is better approximated by a zero-thickness model than by the adiabatic solution within the PSZ (J. R. Rice, 2006).

3.3. Arrhenius Thermal Dependance and Flow Stress

While little is known about rock rheology at large strain rates, stress relaxation occurs through any of i different crystal plastic mechanisms (dislocation diffusion, grain boundary migration, etc.) which generally obey standard Arrhenius thermal dependence with an activation energy Q_j and a power dependence on stress such that

$$\dot{\varepsilon} = A_1\, \tau^{n_1} \exp^{\frac{-Q_1}{RT}} + \cdots + A_i\, \tau^{n_i} \exp^{\frac{-Q_i}{RT}} \tag{9}$$

where the constants A_i may include a grain size dependence for particular deformation mechanisms (e.g., diffusion plasticity). Within a given range of stress and temperature, we assume that a single mechanism will dominate and invert it to obtain

$$\tau_y = C\, \dot{\varepsilon}^{\frac{1}{n}} \exp^{\frac{Q}{nRT}} \tag{10}$$

where σ, $\dot{\varepsilon}$ are the stress and the shear strain rates, respectively and T is the temperature. The exponent may be as low as $n = 1$ for some purely diffusive processes (Nabarro-Herring Poirier, 1985) but in most cases $n > 1$; for example, $n = 2$ for grain boundary sliding (Karato, 2008) and typical values $1.5 < n < 3$ are observed at $\dot{\epsilon} = 10^3 - 10^4$ in experiments on ceramics in brittle conditions (Lankford, 1996). The term C (Pa $s^{1/n}$), though considered constant here for simplicity, may be strongly dependent on grain size (e.g., in the case of grain boundary sliding) among other parameters (Violay et al., 2012). A consequence of $n > 1$ is that the $\dot{\varepsilon}^{1/n}$ term does not vary greatly under extremely elevated values of strain rate (e.g., the term $\dot{\varepsilon}^{1/3}$ varies of about 25% upon a twofold increase of slip velocity from 1 to 2 m/s, assuming a shear zone of 100 μm). On the other hand, expected temperature changes of a few hundred degrees may induce a huge variation in the exponential dependence. As a consequence, under high slip velocity we can expect that the variation of τ_y is primarily due to temperature changes and, for simplicity, we may neglect the variability of $\dot{\varepsilon}^{1/n}$ to write

$$\tau \approx \alpha\, \tau_a \exp^{\frac{T_c}{T+T_i}} = \tau_0 \exp^{\frac{T_c}{T+T_i}} \tag{11}$$

where τ_a is a reference stress $T_c = Q/n\,R$ and α is the real contact area and $\tau_0 = \alpha\tau$. Here, T_c is an absolute temperature (in °K). The term T_i has been added to the denominator, because in the following section T is the background temperature rise with respect to the initial temperature (in the case of the experiments this will be the room temperature $T = 293$°K).

3.4. Local and Background Temperatures

The growth of α with temperature (due to thermal weakening of σ_c) may reduce or even surpass the weakening due to the right-hand term in Equation 11, which may explain the results that no significant weakening is observed under low slip rate even at high temperatures (King & Marone, 2012; Noda et al., 2009). However, the growth of the contact area is controlled mainly by the formation of new asperity contacts (as opposed to the growth of pre-existing ones Persson, 2000), and involves a sensibly deeper-rooted strain in a larger volume than the immediate layer below asperity contact. Consequently, the increase of α should be sensitive to the average increase of the interface temperature, or background temperature T, while the weakening of τ_y will be sensitive to the local, transient temperature peak $T + \Delta T$ reached at the asperity contact, where ΔT is the transient temperature increase in the asperity (Figure 1b). Provided that the slip rate is high, frictional heat has little time to diffuse away from the asperity during its limited contact lifetime; therefore, the excess temperature ΔT will be significant (Archard, 1959; J. R. Rice, 2006). However with continued slip, the local overheating ΔT starts to diffuse away from the asperities and gradually contributes to the rise of the background temperature T.

If the background temperature continues to rise (Figure 1c) at some point the formation of a pervasive layer of amorphous material, melt, wear product, or viscous nanocrystalline material may fill the interstitial space between asperities, as a saturation value of $\alpha \approx 1$ is reached. In case of a continuous lubricant layer, under high velocity the thermal gradient in the vicinity of the slip zone is very steep and an extremely thin (<100 μm), overheated, and low effective viscosity layer develops (Figure 1c). This situation has been documented in the case of frictional melt (Nielsen et al., 2008) and in the case of coseismic viscous flow in coseismic ultramylonites (Pozzi et al., 2019).

Consequently, we may consider that under high slip velocity, the growth of α is initially negligible (i.e., models of flash weakening acting in the very early stages of slip), but gradually increases with the accompanying growth of a pervasive lubricant layer, in which case the lubricant effect will compensate the increase in the contact area and the friction will not increase.

However, the transition from an initial flash heating to a fully developed lubricant layer can be complex and non-monotonic, especially at low normal stress. A relative restrengthening can occur due to the increase of the contact area ratio α with temperature rise, and the straining and elongation of the contact asperities, while voids are filled by-products of comminution, decomposition or cool melt. Microstructures corresponding to such stages were described to some extent for experiments on Gabbro under increasing slip amounts, see Hirose and Shimamoto (2005).

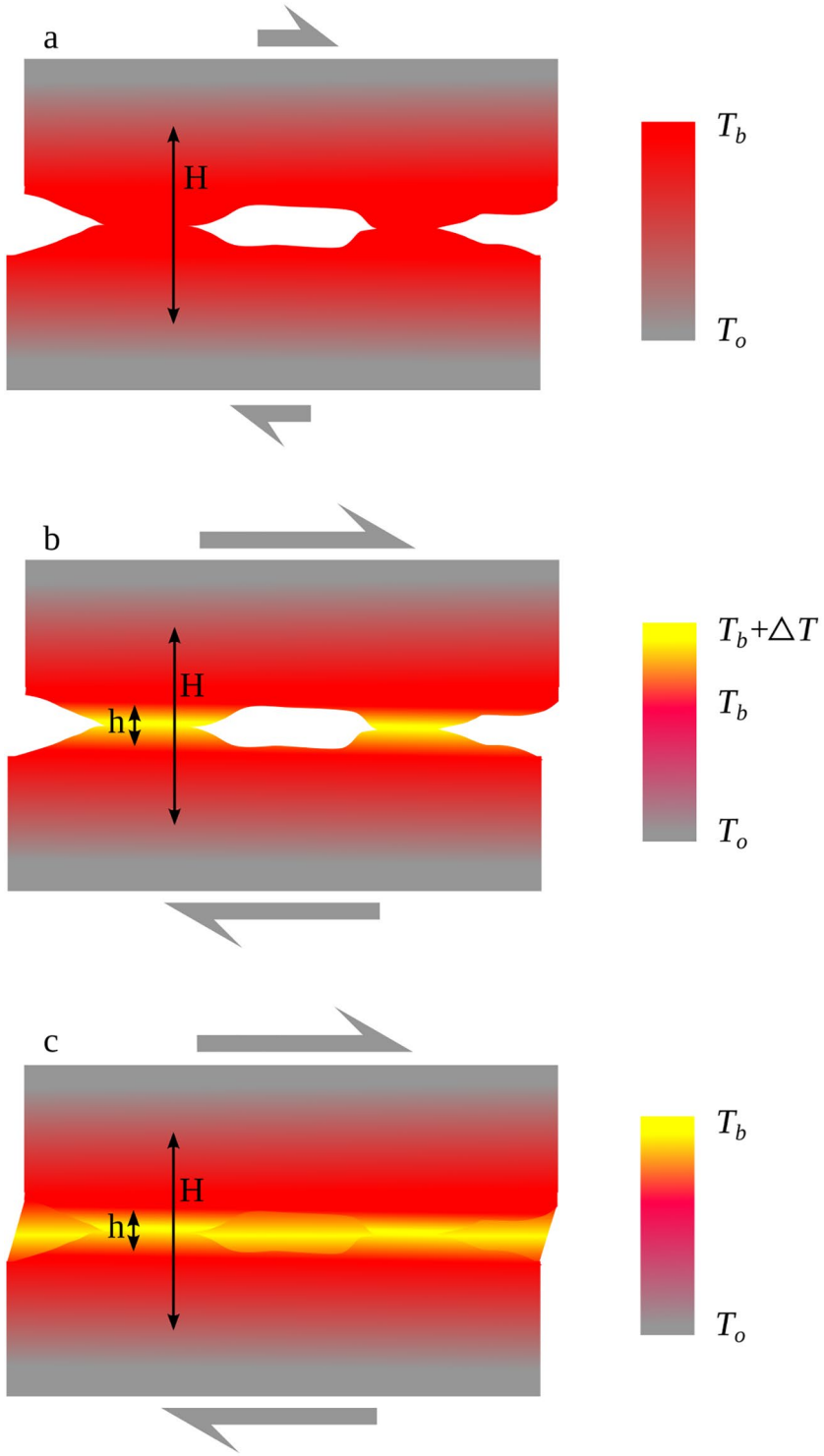

Figure 1. Schematic temperature distribution in the slip zone. (a) Slow velocity: the heat diffuses beyond the asperity size during the lifetime of a contact, the temperature rise is homogeneous within (h) The temperature T_b is evenly distributed, so that weakening is compensated by the growth of the contact area. High velocity: (b) The asperity undergoes a local, transient temperature rise ΔT which diffuses within a limited thickness h during the short contact lifetime; on timescales of multiple contacts, the heat diffuses throughout thickness H and background interface temperature rises to T_b. Temperature is unevenly distributed; the weakening due to highly localized temperature $T_b + \Delta T$ surpasses the friction increase due to the growth of contact area under an average interface temperature T_b. (c) A pervasive layer of overheated, lubricant material has formed with peak temperature $T_b + \Delta T$ within the layer, and weakening is efficient.

3.4.1. Temperature Computation

We provide a number of indications that background temperature plays an important role in the weakening (Section 4). Therefore, its computation is of paramount importance in problems of thermal weakening.

The problem of heat diffusion is well known and a number of analytical and numerical solutions have been proposed. However, not all numerical solutions are equally effective, and inefficiency can be limiting in a problem where temperature needs to be computed repeatedly at many different points (as in the case of dynamic rupture models). For the type of frictional heating problem at hand, we compare the performance and advantages of each of three different numerical solutions of temperature diffusion: (1) discrete summation resolution of the integral solution, (2) a wavenumber formulation, which solution consists in the update and summation of a small number of memory variables, and (3) a finite difference, Crank-Nicolson scheme. Details about the methods and compared performance are found in Appendix A.

4. Signature of Thermal Weakening in the Experimental Data

4.1. Weakening and Temperature Change

The particular scaling of weakening with friction, slip velocity, and frictional power systematically observed in high velocity friction experiments is compatible with a thermal signature. If temperature is the culprit, weakening should be achieved after a slip distance scaling as $u_c \propto 1/(\tau^2 V)$ and after slip duration scaling as $t_c \propto 1/(\tau\, V)^2$, as argued in Nielsen, Di Toro, and Griffith (2010). Indeed for an indicative constant value of shear stress and slip rate, an indicative solution of A1 with constant τV yields a temperature rise $T_c = \gamma\, \tau_c\, V \sqrt{t_c}$ after a time interval t_c, and solving for time yields $t_c = T_c^2 \,/\, (\gamma\, \tau\, V)^2$, where $\gamma = (2\, \rho\, c \sqrt{\kappa\, \pi})^{-1}$. Replacing for slip $u_c = t_c\, V$ we obtain $u_c = T_c^2 \,/\, (\gamma^2\, \tau^2\, V)$.

To illustrate this, we may compare two similar experiments conducted on marble in Figures 2a and 2b, where average frictional power $\overline{\tau\, V}$ differs by about a factor of two, and average $\overline{\tau^2\, V}$ by a factor of six. A similar drop to 1/3 of the initial shear stress is achieved in the two experiments at slip distances which differ by about a factor of six. Similarly, the experiments indicate that weakening time t_c scales roughly as the inverse power squared $(\tau\, V)^2$ as predicted.

An upper bound temperature can be obtained using Equation A1 with no heat sinks, and $\rho = 2{,}700.0$ kg/m^3, $c = 833$ J/K and $\kappa = 0.821\ 10^{-6}$ m^2/s, for mass density, heat capacity, and thermal diffusivity of marble, respectively (Merriman et al., 2018). The estimated T curves are represented in Figure 2, showing that a comparable temperature rise ($T \approx 190$°C) is achieved in both experiments at an equivalent weakening stage. These simple scaling relations seem to reinforce the idea that background temperature T exerts a strong control on the weakening.

However, at a time where weakening is already pronounced, the background temperature is still much too low ($T \approx 210$°C) to trigger melting or decomposition processes (a lower bound ≈ 570°C is indicative of calcite decomposition). A similar observation can be made for the weakening of gabbro (Figure 3), with the example of experiment s555 where pervasive frictional melt formed at advanced stages ($t > 1$ s). Substantial weakening is observed much earlier ($t \approx 0.15$ s). Using $\rho = 3{,}000$ kg/m^3, $c = 715$ J/K and $\kappa = 1.1\ 10^{-6}$ m^2/s for gabbro (Miao et al., 2014), the background temperature estimate is still only ≈ 200°C after weakening to 1/3 of the peak. The expected bulk melting temperature, about 1200°C, is achieved only later in the experiment.

Efficient weakening occurs at consistently lower background estimated temperatures than those expected to induce weakening of the material through decomposition or melting. However, local intensification of heating ΔT well above that of the background temperature T can be achieved if stress is concentrated on a fraction of the contact area only. This concentration mechanism forms the basis of the asperity flash heating (Archard, 1959; J. R. Rice, 2006), one of the frictional models discussed and tested below. In the coming sections, we will define T and ΔT and demonstrate that both are of fundamental importance in the weakening process.

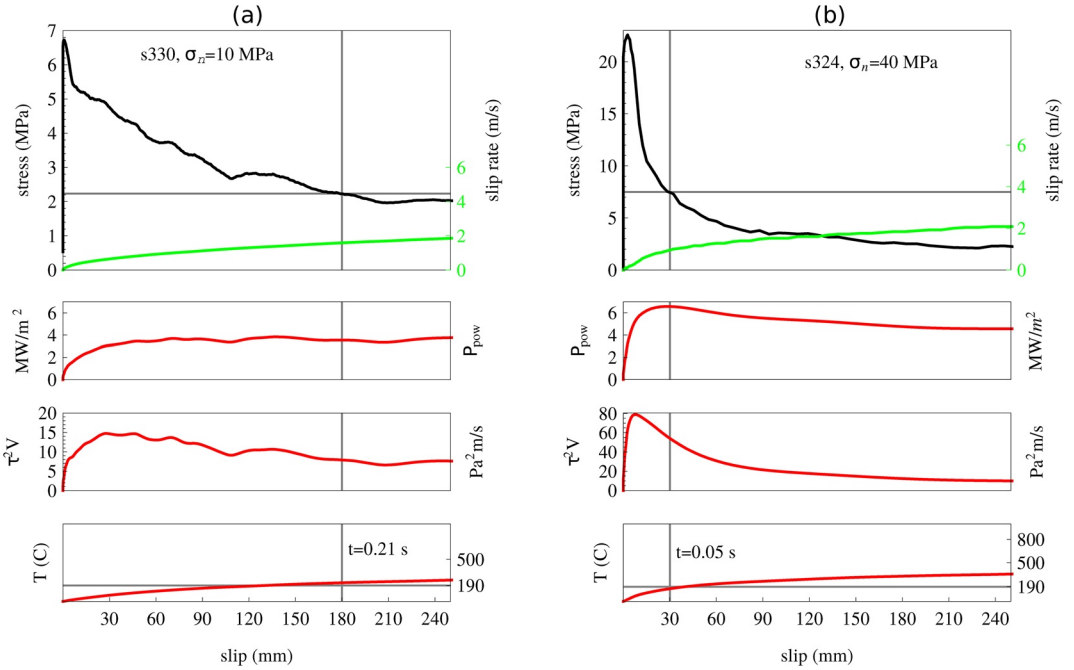

Figure 2. Comparison of two sliding friction experiments on precut Carrara marble performed under identical conditions except for normal stress (10 and 40 MPa, respectively). The weakening curve, the slip velocity, power, and the product $\tau^2 V$ are shown in both cases. (a) Experiment s330 performed at normal stress 10 MPa. The shear stress drops to 1/3 of the peak value (indicated by horizontal line) during the initial 0.21 s and 180 mm of slip (vertical line), with average values $\overline{\tau^2 V} \approx 12\ \mathrm{Pa^2 m/s}$. (b) Experiment s324 performed at normal stress 40 MPa. Shear stress drops to 1/3 of the peak value during the initial 0.05 s and 30 mm of slip, with average values $\overline{\tau^2 V} \approx 70\ \mathrm{Pa^2 m/s}$. A factor of six reduction in the weakening distance corresponds roughly to a factor of six increase in $\tau^2 V$, which is expected if weakening is related to temperature increase. Similarly, the factor of two reduction in average power $\overline{\tau V}$ results in a factor of four increase in time (0.21 and 0.05 s, respectively) to reach equivalent weakening. A similar background temperature increase ($T \approx 190$°C) above initial ambient temperature ($T = 20$°C) is estimated in both experiments at 1/3 weakening; however, a background temperature $T \approx 210$°C is much lower than that expected to trigger weakening by decomposition reactions in calcite (about 600°C). See text for further details.

4.2. Weakening of Nitrogen-Cooled Marble

In Figure 4a, we compare two experiments s876 and s880, performed on solid calcite (Carrara marble) under identical conditions, except that in s880 the rock sample was immersed in liquid Nitrogen for several seconds immediately before the experiment. This is a simple experimental test to verify that the background temperature difference has an effect in line with the prediction of basic dimensional analysis of thermal weakening. Alternatively, the temperature of the sample may have been raised before the experiment, but cooling poses lesser technical difficulties.

Our indicative estimate is that the temperature is $-140 < T_i < -40$°C within 0.5 mm of the sample surface, at the beginning of the experimental sliding. Our estimate assumes that Newton's law of heating applies (with a poorly constrained heat transfer coefficient for air 2.5–25 $\mathrm{W/m^{-2}K^{-1}}$) within the 30 s elapsed between extraction of the sample from the nitrogen and the beginning of the experimental sliding. As a consequence, the initial temperature is lower for s880 than for s876, since the latter was initially at room temperature. If background temperature plays a role in the weakening, we expect to see some delay in the weakening for s880, which we may estimate as follows. Let T_c be the temperature rise achieved in s876 after sliding for about $t = 0.2$ s (at which point the stress dropped at 1/3 of the peak). Reasoning along similar lines as in the previous section we have $T_c = 20 + \gamma\, \tau\, V \sqrt{t}$ (assuming an initial temperature of 20°C). For s880 $T_c = -70 + \gamma\, \tau'\, V' \sqrt{t'}$ (assuming an indicative temperature −70°C). Taking indicative values $\tau \approx 3$ MPa, $\tau' \approx 3.3$ MPa, $V \approx 0.65$ m/s, $V' \approx 0.9$ m/s during the weakening interval, computing γ with the same

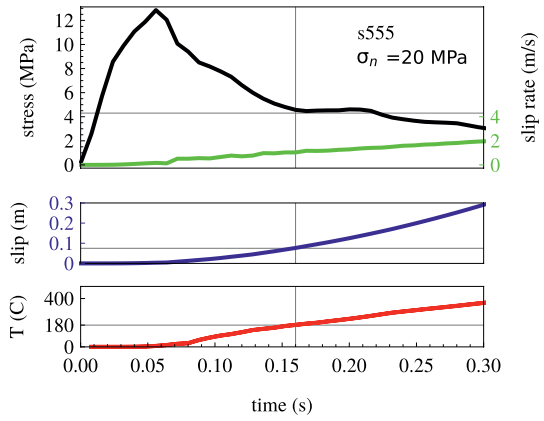

Figure 3. Evolution of shear stress and estimated temperature for experiment s555 performed on gabbro at 20 MPa normal stress. Weakening is initiated at $t \approx 0.05$s. In this experiment, pervasive melt is observed about 1 s after slip initiation; however, consistent weakening (drop to 1/3 of peak stress) precedes the onset of pervasive melt and underestimated background temperatures (ca. 200°C) well below the melting point (ca. 1200°C).

parameters for marble as in the previous section, and equating T_c for both experiments, we obtain $t' = \left(\sqrt{t}\ \tau V\ /\ (\tau' V') + 90\ /\ (\gamma \tau' V')\right)^2 = 0.26$ s, and a delay $t - t' \approx 0.06$ s, which is roughly the delay observed in the experiment. A more accurate computation of the weakening, including the full evolution of T is shown in Figure 4b, yielding similar delay times (the full model is developed in further sections).

5. Test of Thermal Weakening Models

We test the fit of experimental data with two thermal weakening models: a direct Arrhenius thermal dependence, and a model flash weakening (J. R. Rice 2006) which includes both the evolving background temperature and heat sources and sinks. We discuss the differences between flash weakening and frictional melting, and test both thermal weakening models for either.

Two end-member lithologies were tested here, a calcite rock (Carrara marble) and a silicate build rock (microcrystalline gabbro). These show quite different behavior under frictional heating, as gabbro will undergo profuse melting past the initial stages of slip, but not the marble. Therefore, the micromechanics of friction are similar in the initial part of slip, but differ more widely in the later phases, in particular the recovery during the deceleration phase. The flash weakening law (Archard, 1959; J. R. Rice, 2006) was initially proposed as a kinematic treatment and did not consider the frictional recovery. Even so, the inclusion of background temperature allows to reproduces reasonably well the recovery in marble, but it over-predicts the recovery in gabbro. Recovery of marble has been considered in the context of thermal-dependent, diffusion creep plasticity (Violay et al., 2019). Recovery of gabbro has been analyzed in a full model of frictional melting (Nielsen, Mosca, et al., 2010), but we propose here a simplified alternative model which follows an Arrhenius thermal dependence on background temperature.

All numerical replications of the experiments are performed by imposing the experimental slip velocity history and the peak stress (i.e., static friction coefficient times normal stress). The temperature is revised at each time step based on the shear heating power as a heat source, and both thermal diffusion and dissipative heat sinks. (Considering that the friction model should be predictive, the heat source is based on the computed shear stress, not the experimentally measured shear stress.)

Friction laws are based on either two or three parameters, as indicated in the text and the figures. For the solution of temperature diffusion, we include heat sinks due to endothermal phase transitions which follow (6). Rock properties (κ, c, ρ) are fixed for a given lithology (see Table 1), save for the case where thermal dependence is included for κ, c (Section 6).

We find combinations of frictional parameters and heat sink parameters T_s, C_s that provide a reasonable fit to the mechanical data (friction) by trial and error for each lithology. In the case of experiments s308 and s324, we conducted a systematic search on a grid of T_w, B values in the flash weakening model. For each gridpoint, we computed the model friction curve and its misfit (sum of squared differences for all time steps) with the experimentally measured curve, selecting the smaller misfit value and verifying that it did provide a reasonable fit. We repeated the grid search for different combinations of T_s, q_s, including the case where $q_s = 0$ (no heat sink). A trade-off is observed for the combined values T_w, B, on one hand, and the combined values T_s, C_s, on the other hand. (See grid search example in Figure S3). This results in a reasonable fit for models over a range of parameters, only a subset of which is presented here.

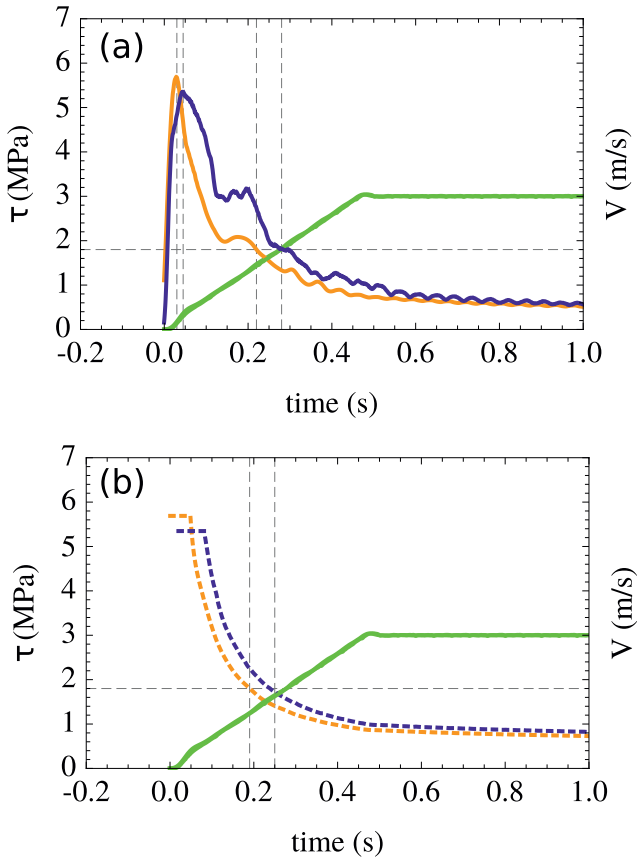

Figure 4. Weakening curves for experiments s876 (yellow curve with earlier peak and weakening) and s880 (blue curve), performed under identical conditions (normal stress 10 MPa, target velocity 3 m/s, acceleration 6.5 m/s^2) except that s880 was previously cooled with liquid Nitrogen, to achieve an indicative temperature of about −140°C (a) Experimental data. (b) Numerical simulation based on the flash weakening with sources and sinks (FWSS) model. A delay of about 0.05 s is observed for 880 in both the experiment and the model.

Table 1
Rock Parameters Used Throughout the Paper Unless Otherwise Indicated

Rock type	κ (m^2 s)	ρ (kg m^{-3})	c (J K^{-1})
Carrara Marble	0.82 10^{-6}	2,700	833
Gabbro	1.1 10^{-6}	3,000	715

Note. κ, ρ, c are thermal diffusivity, mass density and heat capacity, respectively.

5.1. Background Temperature Only: Arrhenius Dependence

From the discussion and the examples of Section 4.1, it is clear that (1) weakening precedes any substantial rise of background temperature; however, (2) the background temperature still plays an important role in the weakening. We first ask the question of how a direct temperature dependence alone is capable of fitting the data where T is the background temperature.

Using Equation 11, a straightforward Arrhenius dependence for the shear stress requires adjustment of two parameters T_c and τ_0. Two additional parameters T_s, C_s are introduced to account for heat sinks (Equation 6) due to endothermal phase transitions. The shear value τ used in the model is the smaller of either that obtained from Equation 11 with the current temperature value, or that of the peak stress $\tau_p = \mu_f \sigma_n$ (where μ_f is static friction coefficient and σ_n is normal stress).

(1) Case of melting (Figure 5). Parameters used for the Arrhenius thermal weakening law (Equation 11) are $T_c = 2700$°K and $\tau_o = 7\ 10^4$ MPa. The parameters used for the heat sink (Equation 6) are $C_s = 40{,}10^6$ Wm^{-2} and $T_s = 2000$°C. We note that a strong trade-off exists between τ_o and T_c in the Arrhenius dependence, whereby increasing τ_c can be compensated by lowering T_c to achieve a very similar result; therefore, such values are purely indicative. The same remark applies to the trade-off between C_s and T_s.

Equation 11 with a single mechanism captures some essential features of fast-slip weakening. However to accurately capture both the very initial weakening and the recovery phase, a combination of strong thermal dependence and large heat sink need to be included, to the point that the background temperature rise remains unrealistically low. This suggests that a simple model of viscous shear heating is not a realistic description of the microscale process. Alternatively, in the case of melting, the heat sink q_s would implicitly incorporate the effect of heat removal by extrusion, which is not accounted for explicitly in this model—as further discussed in Section 6.1. The effect is that the computed temperature T is biased toward lower values.

(2) Case of no melting. We now use the same Arrhenius weakening model but in an attempt to reproduce the case of Carrara marble. A similar approach was adopted in Violay et al. (2019) where plastic deformation of calcite within a thin layer was assumed to follow an Arrhenius-like thermal dependence. In Pozzi et al. (2019), the steady-state friction in calcite was also interpreted in similar terms, and microstructural evidence of plastic flow was provided in support of this high-velocity deformation process. Parameters used for the Arrhenius thermal weakening law (Equation 11) are $T_c = 2000$°K and $\tau_o = 3\ 10^4$ MPa. The parameters used for the heat sink (Equation 6) are $C_s = 50{,}10^6$ Wm^{-2} and $T_s = 2000$°C. As seen in Figure S1 the recovery of friction during the deceleration is severely underestimated, in addition, the temperature again is unrealistically low.

While the Arrhenius dependence is capable of reproducing the main features of frictional melting, it is more problematic to use it in the case of marble where no melting occurs. This is not altogether surprising, as the Arrhenius model assumes the shearing of a layer with temperature-dependent viscosity, a situation well adapted to frictional melting. However,

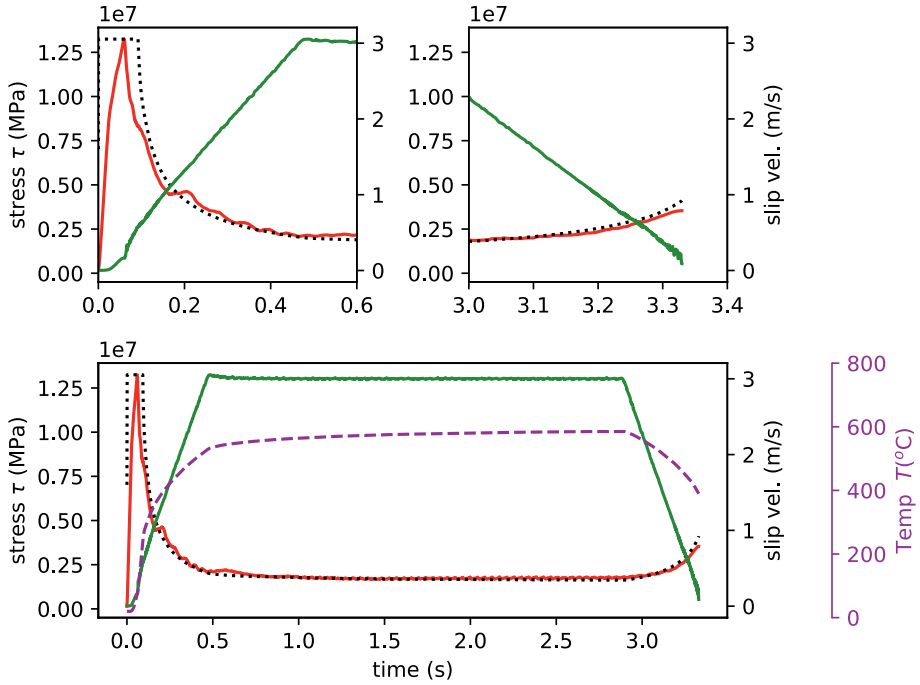

Figure 5. Experimental fit of gabbro friction with Arrhenius thermal weakening and heat sinks (normal stress 20 MPa). Solid red: measured experimental shear stress. Dotted black: Model friction. Solid green: Measured slip velocity. Dashed purple: Computed temperature.

in the case of marble, a model of flash weakening is likely to occur in the initial part of the slip, before the development of a continuous, high-temperature layer of low-viscosity material which can be either melted, as observed in silicate rocks (Nielsen et al., 2008), or not, as observed in carbonate rocks (Pozzi et al., 2019).

5.2. Flash Weakening With Background Temperature Evolution, Heat Sources and Sinks

We explore here a model of FWSS of heat included in the temperature estimation. Flash weakening and heating of contact asperities have been proposed as a model for high-velocity friction evolution (Archard, 1959; Beeler et al., 2008; Rempel & Weaver, 2008; J. R. Rice, 2006). There are strong experimental indications (Acosta et al., 2018; Chen & Rempel, 2014; Goldsby & Tullis, 2011; Tisato et al., 2012; Violay et al., 2014, 2015, 2011; Violay, Nielsen, Gibert et al., 2013; Violay, Nielsen, Spagnuolo et al., 2013) that this model is relevant for high-velocity experiments, in both silicate- and carbonate-built rocks, at least in the first millimeters of a slip or until melting or decomposition of the rock minerals creates an almost continuous, amorphous interstitial layer. One motivation to explore flash heating is that weakening precedes the substantial rise of the background temperature of the sliding interface (as discussed above in connection to Figures 2 and 3). Initial thermal weakening may be achieved only if local temperatures $T + \Delta T$ at asperity contacts are much higher than the background temperature T.

The FW model considers that the lifetime of asperity of linear dimension D is indicatively $t_c = D/V$. For an asperity sheared under incipient yield stress τ_c, the heating results from frictional power $\tau_c V$. Assuming that heat diffusion is mostly perpendicular to the fault, during the asperity lifetime, solution of Equation A1 with $q \approx \tau_c V =$ const. yields the local temperature rise $\Delta T = \gamma \tau_c V \sqrt{t_c} = \gamma \tau_c \sqrt{V D}$, and the time during contact at which the asperity weakens is $t_w = (T_w - T)^2 / (\gamma \tau_c V)^2$. Upon defining a threshold temperature $T_w = T + \Delta T$, a minimum slip rate V_w can be computed at which shear resistance is lost within the duration of an asperity contact lifetime:

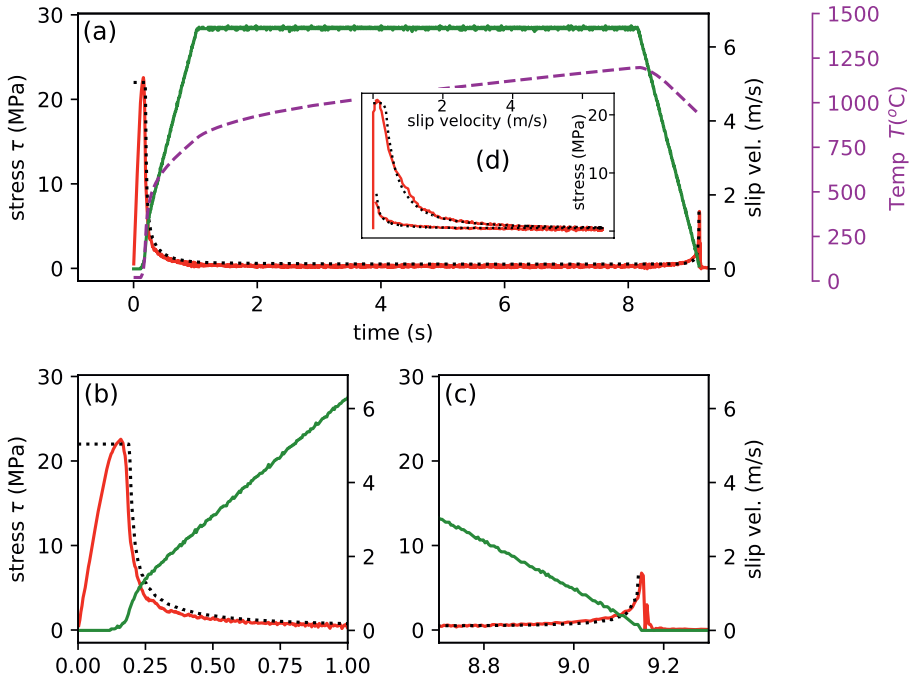

Figure 6. Experiment s324 on Carrara marble, data and model (normal stress 30 MPa, target velocity 6.5 m/s, acceleration 6.5 m/s^2). Same parameters as in Figure 7 (except for the heat sink which was changed to $C_s = 4.5$ 10^6Wm^{-2} instead of 3 10^6). (a–c) Show variables as a function of time, (d) Shows stress versus velocity.

$$\begin{aligned} V_w &= \frac{1}{\gamma^2\,\tau_c^2\,D}\,\mathrm{Max}\Big[T_w - T, 0\Big]^2 \\ &= B\;\mathrm{Max}\Big[T_w - T, 0\Big]^2 \end{aligned} \tag{12}$$

The average strength of an asperity contact during its lifetime will be $\tau_a = (\tau_r(t_c - t_w) + \tau_c t_w)/t_c$, where τ_r is the residual shear stress supported by the weakened asperity. Assuming an asperity population with dominant dimension D, using $\tau_p = \alpha\,\tau_c$, $\tau_w = \alpha\,\tau_a$ and noting that $t_w\,/\,t_c = \tau_c\,(T_w - T)^2\,/\,(\gamma^2\,\tau_c^2\,V\,D) = \tau_c\,V_w\,/\,V$ it is found (Beeler et al., 2008; Rempel & Weaver, 2008; J. R. Rice, 2006) that the effective sliding shear stress is

$$\tau \approx (\tau_p - \tau_w)\left(\frac{V_w}{V}\right) + \tau_w \tag{13}$$

for $V > V_w$. The flash weakening friction is adjusted with the three parameters B (°C^{-2} ms^{-1}), T_w (°C) and τ_w (Pa). The shear value τ used in the model is the smaller of either that obtained from Equations 12 and 13 with the current temperature value, or that of the peak stress $\tau_p = \mu_f \sigma_n$.

In previous models, the variation of the background temperature T is often neglected in Equation 12, with the consequence that V_w remains constant (Goldsby & Tullis, 2011; Noda et al., 2009). Indeed the direct numerical computation of T with classical methods can be rather costly and inefficient. However, T increases substantially after the first millimeters of slip as shown in Figure 2, and unless evolution of T is included, flash weakening fails to reproduce accurately the friction recovery observed in the experiments. One immediate evidence that friction is not purely velocity dependent is the lack of symmetry in the acceleration and deceleration phase, whereby an hysteresis loop is observed—see, for example, the τ versus V representation in Figure 6d, and also experiments reported in previous studies (Goldsby & Tullis, 2011; Proctor et al., 2014). Thus, inclusion of background temperature, which is substantially higher in the recovery phase than in the weakening phase, allows to moderate the velocity effect by acting as a state variable. This allows to obtain a hysteresis cycle where the initial weakening and the final recovery are not symmetrical, and are not purely

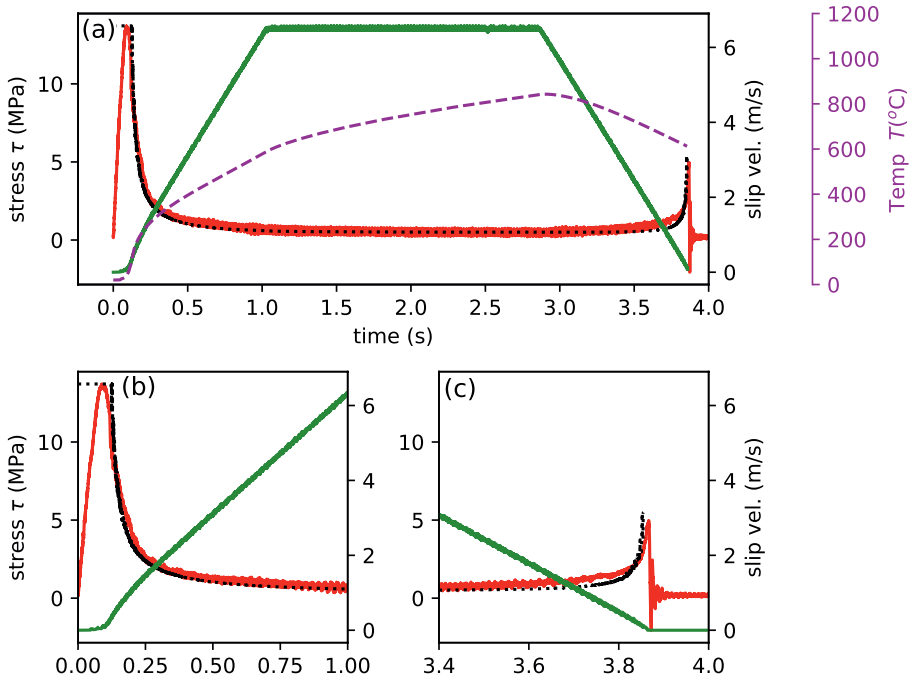

Figure 7. Experiment s308 on Carrara marble, data, and model (normal stress 20 MPa, target velocity 6.5 m/s, acceleration 6.5 m/s^2). Shear stress in an experiment (red) and in model FWSS (black dashed); imposed slip velocity (green). Temperature evolution (modeled) including heat sinks (purple dashed). (a) is the whole experiment and (b)–(c) are zoom of start and end. For marble, parameters of rock, FWSS, and heat sinks are indicated in the text. FWSS, flash weakening with sources and sinks.

velocity dependent. The higher temperature at the end of the experiment allows the friction recovery to be relatively slower, as observed.

In addition, we note that an accurate evolution of T should include both heat sources (frictional power τV) and any significant heat sink (other than diffusion). Heat sinks are not triggered at the beginning of the slip, when the background temperature is still low; thus, they do not affect the initial temperature rise and weakening. However, as slip advances and more heat is produced, the heat sinks allow to buffer the temperature rise (Brantut et al., 2010; Sulem & Famin, 2009). We show that the temperature modulation induced by heat sinks has a sensible effect on the recovery of friction during slip deceleration.

The FWSS law is based on the full set of Equations 3, 6, 12, and 13; the only input variable is the slip velocity $V(t)$. Input parameters are (1) the group $\gamma^2 \tau_c^2 D$ (with dimensions [L T^{-1}], allowing the definition of a characteristic velocity V_w), (2) the peak stress τ_p (which may be predicted using $\tau_p = \mu \sigma_n$) and residual stress τ_w (for computation of τ), and (3) C and T_s (for a single dominant heat sink).

One of the peculiarities of the model described by Equation 13 is the absence of explicit dependence on normal stress. However, taking into account the evolution of background temperature T, with τV as a heat source implicitly includes normal stress. Indeed during the initial part of the slip $\tau = \tau_p = \mu_s \sigma_n$ where μ_s is the initial friction coefficient (of the order of 0.6 before the onset of weakening), so the heat production rate is higher if the normal stress is higher. On the other hand, if the initial (peak) stress is higher under higher normal stress, temperature rise and weakening will be accelerated by a similar proportion. As a consequence, the weakening slip distance and the fracture energy may not be significantly altered by a change in normal stress. This behavior was indeed observed in a synthesis of different high-velocity friction laboratory experiments (Nielsen, Spagnuolo, Smith, et al., 2016; Nielsen, Spagnuolo, Violay, et al., 2016).

In Figures 7–9, we compare the FWSS model to experiments performed on samples of solid carbonate (Carrara marble). Notably, the shear stress curves in the weakening, steady-state, and recovery phases are

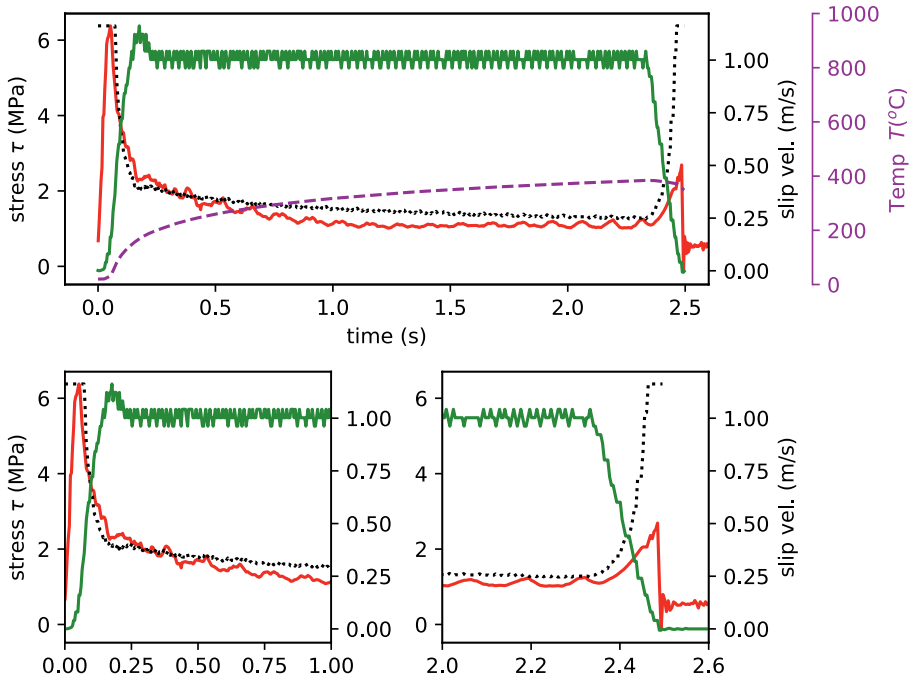

Figure 8. Experiment s257 on Carrara marble, data, and model (normal stress 10 MPa, target velocity 3 m/s, acceleration 3 m/s^2). Same parameters as in Figure 7.

reasonably well matched with the same set of parameters although the three experiments are different in terms of loading conditions (normal stress and target slip rate).

An interesting test of the robustness of the model is whether the outcome of different experimental conditions (normal stress, slip velocity) can be reproduced with a single set of parameters. We show the result

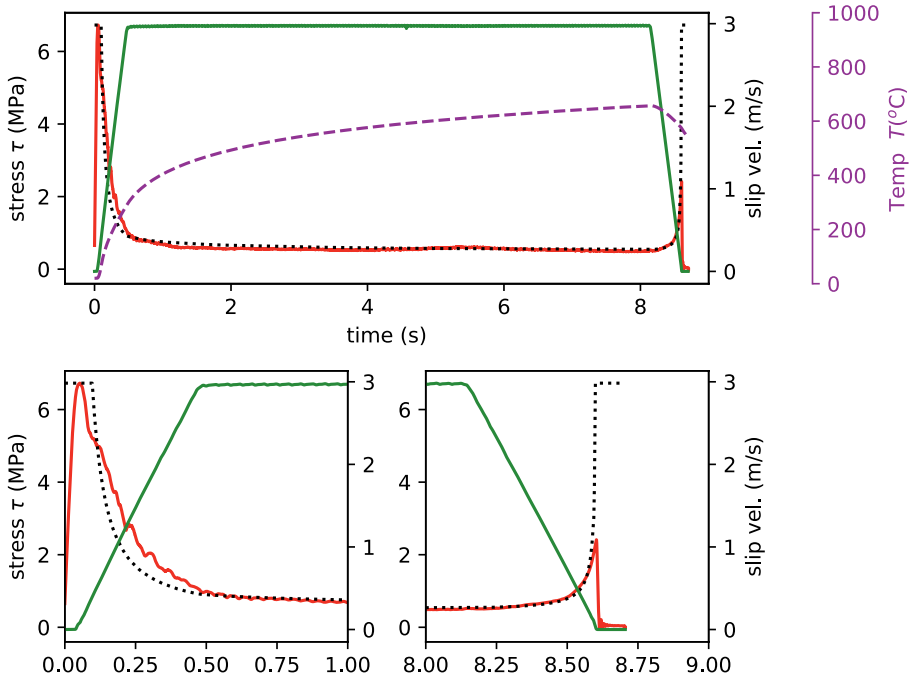

Figure 9. Experiment s330 on Carrara marble, data, and model (normal stress 10 MPa, target velocity 3 m/s, acceleration 6.5 m/s^2). Same parameters as in Figure 7.

in four different experiments in Figures 7–9, and in most cases the weakening, steady-state, and recovery are all reasonably well reproduced with a single set of parameters. The parameters for flash weakening (Equations 12 and 13) are $T_w = 800$°C, $\tau_w = 0.5\ 10^6$ Pa, $B = 0.85\ 10^{-}6$°C^{-2} ms^{-1}. The parameters used for the heat sink (Equation 6) are $C_s = 3\ 10^6$ Wm^{-2} and $T_s = 1700$°C. One exception, though, is experiment s324 which was performed under the most extreme frictional work rate (highest normal stress and slip velocity combination). In this case the heat sink parameter C_s had to be increased by 50% ($C_s = 4.5\ 10^6$) to reproduce correctly the recovery. One possible interpretation is that loss by combined radiation and Newton's cooling is substantial in this experiment, due to the large rate of heating, introducing additional sinks.

If the heat sinks are excluded, the final temperature is much larger (Figure 11c). This reflects on the friction, in particular, on the recovery phase which is underestimated if the same frictional parameters are maintained (Figures 11a and 11b). Note that an equally reasonable fit can be found without heat sink, but by adjusting frictional parameters for each individual experiment (Figure 11c), with a loss of generality in the model.

Indeed, we could not find a single combination of parameters that would fit different experiments for a given lithology, unless we do include heat sinks in the model. Therefore, we posit that the accurate reproduction of a range of experiments, including the recovery phase, can only be achieved with background temperature evolution due to both sinks and sources. A similar observation applies to models including the thermal dependence of κ, c (see Section 6), where a reasonable fit can be obtained both with and without heat sinks provided that the frictional parameters T_w, B are modified for each individual experiment.

6. Effect of Thermal Dependence of Diffusivity and Capacity (κ, c) on Temperature and Friction

We use experimental data from Merriman et al. (2018) on Carrara Marble to derive an empirical dependence on temperature of diffusivity and heat capacity (see supporting information). Although diffusivity and heat capacity are affected in opposite ways by the temperature rise, their combined effect still results in a significant net decrease in the conductivity ($k = \rho\, c\, \kappa$) at relatively high temperatures. However, during high-velocity frictional sliding, the high temperatures are usually reached within a small boundary layer, with a strong negative temperature gradient, because the duration of the slip is short and the diffusion distance is limited. Therefore, it is difficult to predict how important the effect of thermal dependence can be in this context, if not performing a full computation (Figure 10).

To do so requires to take into account the inhomogeneous temperature as a function of depth z from the sample surface, and, therefore, the inhomogeneous spatial distribution of the conductivity/diffusivity parameters, in addition to their change in time. Sadly, in the wavenumber solution, the product of two spatial dependent variables (κ and $\partial_z^2 T$) results in a cumbersome convolution which would nullify the advantage of its efficiency. However, the inhomogeneous solution is manageable by using a numerical method where both time and spatial steps are explicitly defined. To this end, we use a finite difference, the Crank–Nicolson diffusion scheme used previously for frictional heating problems (see Nielsen, Mosca, et al., 2010, and references therein).

Using the conditions of experiment s308, we compare the temperature and shear stress evolution between (1) a model including thermal dependence and (2) one with no thermal dependence, but with equal heat sinks in both. Finally, we repeat the simulation with thermal dependence but increase the amount of heat sink in parameter C_s.

The result in terms of temperature evolution shows that under comparable frictional power curves, the temperature difference introduced by the thermal dependence is substantial (up to about 350°C at the temperature peak). If other parameters (frictional parameters, heat sinks) are kept equal, the difference between models with variable or constant thermal parameters differs largely toward the end of the frictional curve, in particular during the recovery phase (Figure 11b). The net decrease of conductivity, resulting in a higher background temperature, is sufficient to prevent the strength recovery in the flash weakening friction.

However, both models with or without κ, c thermal dependence can reproduce reasonably the frictional curve by adjusting the frictional or the heat sink parameters. For example, by increasing the heat sinks in

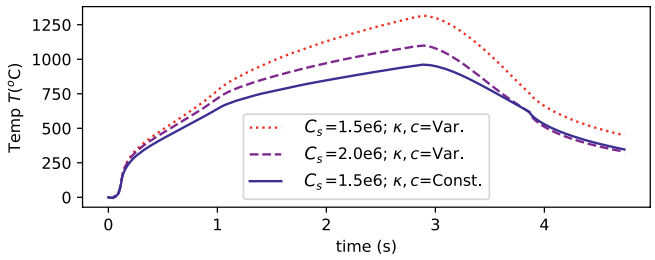

Figure 10. Effect of thermal-dependent diffusivity and heat capacity κ, c. Temperature evolution was obtained with a similar frictional heat input, but for three different thermal models. (1) Thermal dependence of κ, c is allowed and $C_s = 1.5$ MW m^{-2} (dotted red curve). (2) Constant κ, c and $C_s = 1.5$ MW m^{-2} (solid blue curve). (3) Thermal dependence as in (1), but with the heat sink parameter increased to $C_s = 2.0$ MW m^{-2} (dashed purple curve). At high temperature, the heat conductivity is lower, but the energy sinks are more effective, inducing a competing effect on the temperature rise. This allows to obtain similar results in (2) and (3) by adjusting C_s to compensate for the effect of the variable κ, c.

the model with κ, c thermal dependence to $C_s = 2\ 10^6$ MW m^{-2}, the temperature rise is buffered and is closer to that obtained in the model with no κ, c thermal dependence (where $C_s = 1.5$ MW m^{-2}). As a result, both models produce a similar frictional curve, compatible in both cases with the experimental observation (Figure 11a).

Finally, we show that a model with no heat sinks ($C_s = 0$) and variable κ, c also fits the data, provided that the frictional parameters are altered to (T_w, B) = (3800°C, 0.02 10^{-6} ms^{-1}C^{-2}) to compensate for the much higher temperature (Figure 11c). (Such a high value of T_w largely above the weakening temperature of the rock-constitutive minerals, reinforcing the point that if heat sinks are ignored a realistic solution is not achieved.) These results were obtained by conducting simulations with 22 different combinations of (T_w, B) and selecting the outcome with the best fit (also see discussion at the beginning of Section 6).

In conclusion, by adjusting the frictional parameters (T_w, B) for each individual experiment, it seems possible to reach a reasonable fit for either variable or constant κ, c and either including heat sinks or not. However, a robust frictional model should reproduce a combination of different experiments with the same parameter set. This is better achieved by adding the presence of heat sinks and using a single combination of (T_w, B, C_s, T_s) for all experiments conducted on the same rock type. In addition, the effect of variable κ, c can be emulated in models with constant κ, c by lowering the power of heat sinks (parameter C_s).

Note that variations of mass density ρ will also occur due to thermal expansion, but are of second order in this analysis (e.g., less than 1% for granite under a temperature change of 1000°C, Richter and Simmons (1974)).

6.1. Flash Weakening Followed by the Formation of a Viscous Shear Layer

A model for frictional melting has been proposed for both steady-state (Nielsen et al., 2008) and transient (Nielsen, Mosca, et al., 2010) behavior. It accounts for the advancement of a melting boundary (solution of a Stefan problem) and the possibility that melt extrusion occurs through lateral injection veins (natural faults, Di Toro et al., 2005) or at the edges of the sample (experimental simulated faults: Niemeijer et al., 2009; Violay et al., 2014). We will only revisit some features of such a model here, and test to what extent a simpler flash weakening model differs from the melting dynamics.

In the case of frictional melt with extrusion, the thermal balance is quite different from that resulting in (2) from simple diffusive temperature. Apart from the heat loss due to phase transitions already discussed above, there is a radical change in the thermal diffusion equation with an additional convective term as a consequence of the advancement of the melting front into the rock. If we choose to attach the coordinate frame to the moving boundary, we can write:

$$\partial_t T = \kappa\, \partial_z^2 T + v\, \partial_z T + \frac{\delta(z)\, q}{\rho\, c}. \tag{14}$$

where v is the current velocity at which the melt boundary is advancing into the solid. (We recall here that while the melt front is advancing, most of the excess melt produced is extruded, so that the shear heating remains confined in a thin melt layer.) Heat sinks due to phase transitions in this case are essentially due to melting latent heat L such that $q_s = v\, \rho\, L$. Thermal diffusion solutions with a moving boundary are known as the Stefan problem. It can be assumed that the boundary between melt and solid rock is at the melting temperature T_m. As a consequence, v can be computed by applying the boundary condition that $T = T_m$ and $\partial_t T = 0$ at the melting boundary ($x = 0$).

One key process in the presence of melting and extrusion is the advancement of the melting front which counteracts the advancement of thermal diffusion. In the absence of melting and extrusion, as in the case of flash weakening, the background temperature T is representative of recent frictional power dissipated

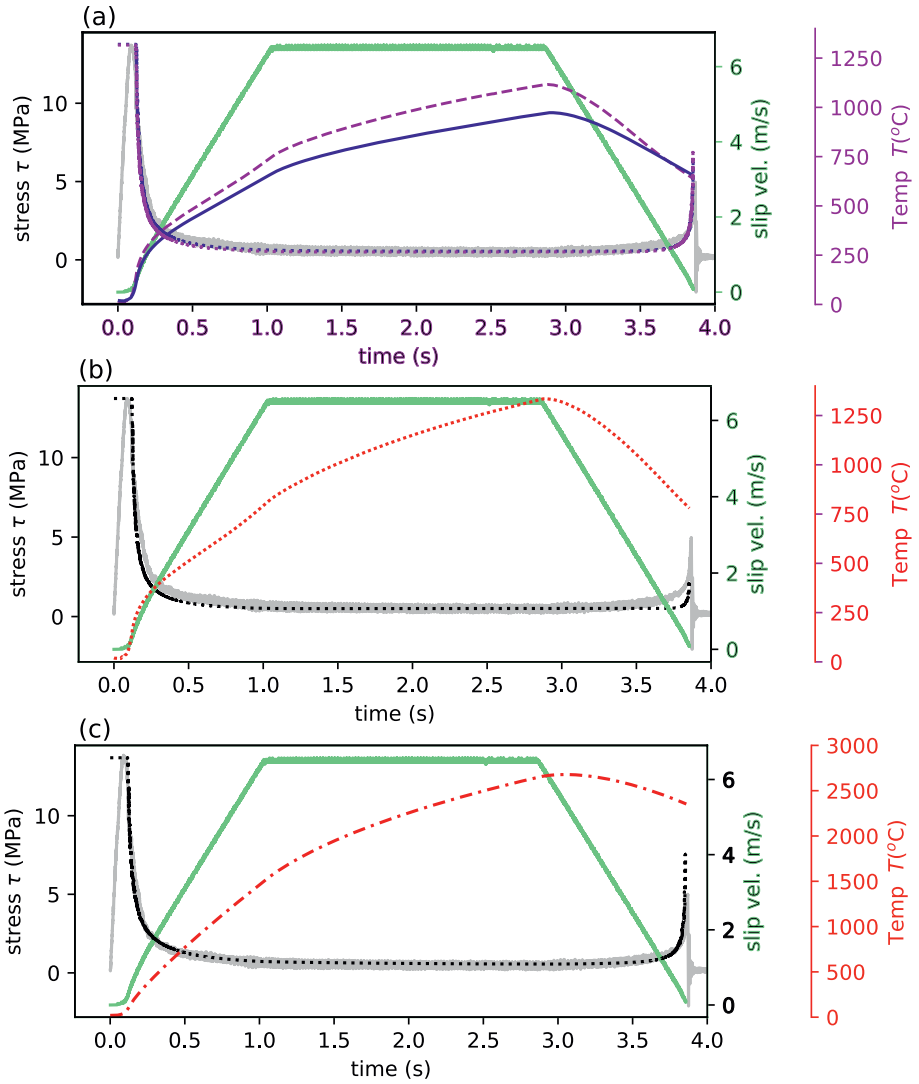

Figure 11. Effect of thermal-dependent diffusivity and heat capacity κ, c on temperature ad shear stress evolution. (a), (b) Same models as shown in Figure 10. (c) An additional model with no heat sink. In (a), the blue and purple dotted curves show simulated stress evolution for models (2, 3) of Figure 10, respectively. *Note*. that both models have a very similar outcome in terms of frictional evolution. (Gray solid curve is experimental stress. Solid blue and dashed purple represent temperature. Light green curve is experimental slip velocity.) In (b), the black dotted curve indicates simulated stress evolution for model (1) of Figure 10, and the red dotted curve is temperature. In (c), we show results for a model with no heat sinks ($C_s = 0$) and variable κ, c, but here, the substantially higher temperature requires a different combination of friction parameters ($T_w = 3{,}800$, $B = 0.02\ 10^{-6}$) to fit the shear stress evolution reasonably well.

on the fault, which induces heating within a finite thickness around the slip zone. Therefore temperature may be considered as a state variable storing the memory of the frictional heating history. However, the advancement of a melting front combined with extrusion will constantly reset the heat stored around the slip zone. The boundary will remain at the melting temperature $T \approx T_m$. Super-heating above T_m may occur within the melt reaching a maximum at the center of the melt layer (Nielsen et al., 2008), but melt is rapidly extruded. Heat diffusion penetrates to an indicative depth $z = 2\sqrt{\kappa\, t_r}$ within a given time interval t_r. Given a shortening rate v (melt front advancement) the typical time of residence of the heat in the rock adjacent to the slip zone will be $t_r = z/v$ resulting in $t_r = 4\,\kappa/v^2$ upon substitution of z. Therefore, the thermal memory of the system is reset over times of the order of t_r, that is, a few seconds, assuming shortening rates of 1 mm/s and standard diffusivity values.

As discussed in Section 4.1 and in Figure 3, it appears that weakening precedes the bulk melting temperature. Therefore, we assume that the initial part of the weakening, before pervasive melt starts, is due to flash weakening behavior and can be modeled as such.

At later times, when pervasive melt and extrusion occur, a full steady-state condition may be reached, as predicted by the model of Nielsen et al. (2008) and experimentally confirmed by Violay et al. (2014). Such a steady state is not reached as rapidly in the absence of a migrating boundary. Only an apparent steady state is reached, later, in the presence of heat sinks q_s (Equation 2), which inhibit the temperature rise is temporarily but only as long as the decomposition products are not depleted in the host rock. Therefore, the boundary migration needs to be included explicitly for an accurate temperature evolution; however, temperature diffusion in the presence of heat sinks does allow reproduce the appearance of a steady-state solution (the background temperature reaches a plateau, although the temperature diffusion continues to progress).

Finally, we note that the frictional recovery during the deceleration phase is expected to differ between flash weakening and frictional melt, although in both cases the sliding surface will undergo irreversible transformation at high slip velocity (phase transitions due to heat, roughness change through abrasion), and in both cases, the background temperature is higher at the end of sliding than at the beginning.

Ideally, in the occurrence of melting, a mixed model should be used with a transition from flash heating to frictional melting after the background temperature reaches T_m. Such a transition can be rather complex, and several experiments show that there is a partial frictional recovery at that stage (Hirose & Shimamoto, 2005), although it is less pronounced in experiments performed at higher normal stress (Hung et al., 2019).

We do not implement here the mixed flash heating/frictional melting model which is a complex task and requires a separate study. However, we show to what extent frictional melt can be approximated either by a simplified Arrhenius dependence (Figure 5 and discussion in Section 5.1), or by the flash weakening law of Section 5.2 (an example is shown in Figure S2). We find that with Arrhenius dependence, a reasonable fit of the stress curve is obtained only with models resulting in unrealistically low temperatures at the interface. On the other hand, flash weakening alone does not predict the recovery accurately in the presence of melting.

A mixed model can be developed also in the case of calcite, where an initial flash-weakening process is followed by the formation of a continuous viscous layer which undergoes high-velocity plastic shear, as posited in Violay et al. (2019) for bare surfaces in frictional contact. Where the slip initiates within a gouge, the eventual formation of a viscous layer after several mm of slip is also observed by Pozzi et al. (2019); however, the initial weakening includes a slip hardening phase. A microstructural evolution with complex processes is observed before the viscous shear is mature. This process is arguably difficult to represent with a flash weakening model.

Finally, a mixed model would also be indicated in the case where fluids are initially permeating the fault surface allow for elastohydrodynamic weakening: as slip accelerates, a transition between three lubrication regimes (boundary, mixed, and fully lubricated regimes) will occur as discussed in Cornelio et al. (2019).

7. Conclusions

We investigated different versions of thermal dependent, high-velocity friction models and tested how well they could be adjusted to replicate a number of experimental observations. Each friction law and each set of parameters was tested against several experiments, conducted under different normal stress and slip velocity, to verify whether the fit was robust under different conditions. We considered aspects of computational efficiency, the role of energy sinks, and the effect of thermal dependence on diffusivity and heat capacity.

The computation of temperature diffusion can be numerically costly, in particular foreseeing its use in models of an extended fault surface where T needs to be tracked at a great number of points. Therefore, we test and compare different methods: the simple discrete summation of the analytical solution, the discrete wavenumber transform, and a Crank–Nicolson finite difference scheme. We find that the two latter methods

are comparable in terms of speed, for the problem to be solved in the case of frictional heating, and that both are much more efficient than the simple discrete summation of the analytical solution. In addition, the explicit spatial grid of the finite differences scheme allows to consider local variations of parameters. We took advantage of such a feature to investigate the thermal dependence of diffusivity and heat capacity.

We include additional heat sinks with an Arrhenius reaction rate, due to endothermal phase transitions are triggered under frictional heating. The temperature evolution is affected, in particular in the final phase of frictional recovery.

Diffusivity and heat capacity, often considered as constant, can undergo important changes when temperatures reach a substantial fraction of the melting temperature. We include such thermal dependence and show that it can have a substantial effect on the temperature and frictional evolution in problems of frictional heating. However, by altering the frictional parameters or the amount of the heat sinks, an effect similar to such thermal dependence can be simulated even in models which exclude it. Interestingly, J. R. Rice (2006) argued that the use of constant thermal properties as constant may be justified if such properties were considered as an equivalent average over a given thermal profile. However, here the thermal properties evolve with temperature, so that they will not only vary spatially but also change in time. Because the heat sinks will be activated only when temperatures are high, concomitantly with the expected drop in thermal conductivity, the time variation is best emulated by decreasing the effectiveness of sinks (C_s) as illustrated in Figures 10 and 11.

For models of flash weakening, we illustrate the existing trade-offs between frictional parameters, heat sinks, and the presence of thermal dependence of the parameters.

In addition to the flash weakening model, we investigate a simplified model including direct Arrhenius dependence of friction on background temperature. Such a model captures some of the main features of the weakening, however fails to account for the initial rapid weakening. A flash weakening model, instead, captures well the initial weakening; however, it requires to include the evolution if the background temperature to reasonably reproduce friction from start to end.

We discuss the differences between flash weakening and profuse frictional melting. It is known that both can take place within a single slip episode, with the flash heating occurring at the start. Given the differences between flash weakening and frictional melting processes, an accurate representation should include both, and then model the subtle transition from one to the other, an endeavor that we leave for future work. However, as an approximation, we show here that a flash weakening model including thermal dependence with heat sources and sinks is able to reproduce cases of frictional melting reasonably well over the limited interval of parameters of the experiments shown here in support.

Finally, we note the experiments presented here are limited to precut, cohesive rocks of two end-members (Carrara marble, gabbro) under dry conditions. One needs to consider that rupture on natural faults will develop in different lithologies, including clays. In addition, deformation of natural faults develops in more complex ways, including diffuse strain, gradual localization of slip within an initially thick fault gouge, multiple branching of rupture, and other dissipative processes which take place off-fault. Fault deformation, therefore, develops in part within a volume rather than only by slip across a surface or by shear of a thin gouge layer. The off-fault deformation and dissipation contribute to the energy balance and to the stress–strain relation, an aspect which needs to be integrated somehow with the frictional slip on the fault for realistic modeling, in ways which are not yet defined. Until then, such limitations need to be kept in mind when using laboratory-derived friction laws in earthquake models.

Appendix A: Comparison of Different Temperature Solution Methods

A1. Direct (Inefficient) Temperature Computation

One well-known (Carslaw & Jaeger, 1959) solution of Equation 2 yields the temperature on the slip plane (where the frictional heat is produced):

$$T(t) = \gamma \int_0^t \frac{q(t')}{\sqrt{t - t'}}\, dt', \tag{A1}$$

where $\gamma = (2\,\rho\, c\sqrt{\kappa\,\pi})^{-1}$ (with mass density, heat capacity and thermal diffusivity ρ, c, and κ, respectively. t is the current time and t' is the integration variable). Direct discretization of A1 with time step δt yields at the n_{th} iteration (time $t = n\delta t$):

$$T(n) = \gamma \sum_{i=1}^{n} \frac{q(i) + q(i-1)}{2\sqrt{\delta t \times (n - i + 1/2)}}\, \delta t. \tag{A2}$$

(implemented using a simple trapezoidal rule for sake of comparison). While Equation A2 may be used to compute temperature, the summation from $i = 1$ to n needs to be repeated for each time n, which is unpractical and inefficient. Another option is to use finite differences or finite elements and solve diffusion explicitly at a number of points (elements) at various distances away from the fault. However in this case a large number of points may be needed to avoid finite model size effects, and this number will increase as the square root of the computation duration, because the diffusion distance scales with $\sqrt{\kappa\, t}$. The advantage of the latter methods is to allow for local variations of conductivity, eventually depending on temperature changes. But in case that small time steps are required, and an extended fault is modeled with inhomogeneous distribution of T and τ, the computation may become prohibitively long. Typical simulations would require the memory storage of a number of time iterations in excess of several thousand. Noticing that Equation A1 is a convolution on may suggest the use of FFT (Fast Fourier Transform) in time. However, the operation would still imply several thousand time iterations n and normally requires that n is a power of 2. Finally, The operation and the storage would take place at each of the subsegment of the modeled fault, which easily exceed the thousands. In conclusion, it is necessary to design an adequate approximation of thermal diffusion. In the section below, we propose a straightforward time iterative scheme, where the temperature is computed to a satisfactory approximation by the use of a small number of memory variables which arise in a discrete wavenumber solution.

A2. Wavenumber Temperature Computation

The one-dimensional heat diffusion Equation 2 with a heat source flux $q = q(t)$ at $x = 0$ per unit time per unit area, which we re-write here for convenience, states:

$$\partial_t T = \kappa\, \partial_z^2 T + \frac{\delta(z)\, q}{\rho\, c} \tag{A3}$$

where $\delta(.)$ is the Dirac delta function and z is the distance from the slip surface. Taking the wavenumber transform $z \to s$, we note that the temperature is an even function of z and—expecting no singularities—we may use the Cosine Fourier transform (using only the positive real wavenumbers) to obtain

$$\partial_t \theta(s, t) = \frac{q(t)}{\rho\, c} - \kappa\, s^2\, \theta(s, t) \tag{A4}$$

where $\theta(s, t)$ is the wavenumber Fourier transform of $T(z, t)$. The use of the wavenumber transform in the direction perpendicular to the fault (here z) for the solution of rupture and friction problems was first proposed by Noda and Lapusta (2010).

For consistency, we show in Appendix B how the analytical expression of temperature (Equation A1) can be retrieved by solution of Equation A4 and the subsequent inverse cosine transform. However here, we directly update θ using a discrete wavenumber summation. For the discrete version of time-iterative scheme, it is better to select a backward Euler stepping scheme to insure stability (backward meaning that the updated value $\theta(s, t)$ is both on the right- and left-hand side of the equation):

$$\frac{\Big(\theta(s,t)-\theta(s,t-\delta t)\Big)}{\delta t}=\frac{q(t)}{\rho\, c}-\kappa\, s^2\;\theta(s,t)\,. \tag{A5}$$

to the first order of the series expansion. By regrouping terms, we obtain the updated value as

$$\theta(s,t)=\left(\frac{q(t)\,\delta t}{\rho\, c}+\theta(s,t-\delta t)\right)\frac{1}{1+\delta t\;\kappa\, s^2}\,. \tag{A6}$$

The update of $\theta(t)$ is obtained from the former value $\theta(t-\delta t)$ plus the scaled heat rate, divided by a constant function of wavenumber s. Importantly, the summation does not require all past times, but only the value of θ from the former time step. The inverse transform (i.e., summation over s) yields temperature such that

$$T(x,t)=\frac{2}{\pi}\int_0^\infty \cos(s\;z)\;\theta(s,t)\;ds, \tag{A7}$$

and at $z=0$:

$$T(0,t)=\frac{2}{\pi}\int_0^\infty \theta(s,t)\;ds\,. \tag{A8}$$

For the numerical solution, we also discretize the wavenumbers by steps δs. We shall use the notation $\theta_m(t)=\theta(m\;\delta s,\,t)$ with $(1<m<M)$ where M is the total number of discrete wavenumbers. Thus, Equation A8 yields:

$$T(t)=\frac{2}{\pi}\sum_{m=1}^{M}\theta_m(t)\;\delta s \tag{A9}$$

and each θ_m variable will be computed according to Equation A6 such that

$$\begin{aligned}\theta_m(t) &= \left(\frac{q(t)\,\delta t}{\rho\, c}+\theta_m(t-\delta t)\right)\frac{1}{1+\delta t\;\kappa\, s_m^2},\\ &\text{where}\\ s_m &= (m-1\,/\,2)\,\delta s.\end{aligned} \tag{A10}$$

A rather small summation number M is sufficient. The choice of suitable δs and M is discussed further below. The time integration has disappeared, replaced by a more convenient summation over a small number of memory variables from the previous time step. The constitutive relation may be now written as (1) a friction law based on M memory variables and (2) an evolution law for the memory variables:

$$\tau(t)=f(\theta_1+\theta_2+\ldots\theta_M,V,\ldots) \tag{A11}$$

$$\partial_t\theta_m=\frac{q(t)}{\rho\, c}-\kappa\, s_m^2\;\theta_m\quad\Big(\text{where } s_m=(m-1\,/\,2)\,\delta s\Big) \tag{A12}$$

The memory variables here have temperature dimension (as opposed to time dimension in the case of Dieterich-Ruina rate and state evolution friction laws). The interpretation of the solution in memory variables corresponding to different wavenumbers is straightforward: the largest wavenumbers represent the fast temperature evolution due to thin penetration depth of heat, while the small wavenumbers represent the slower temperature evolution due to larger penetration depth.

Using Equation A9 rather than Equation A2 will require a fixed, limited number M of memory variables in a short summation as opposed to an ever-increasing number of temperatures stored from each previous timestep (see example below, with $M=16$ and $M=32$).

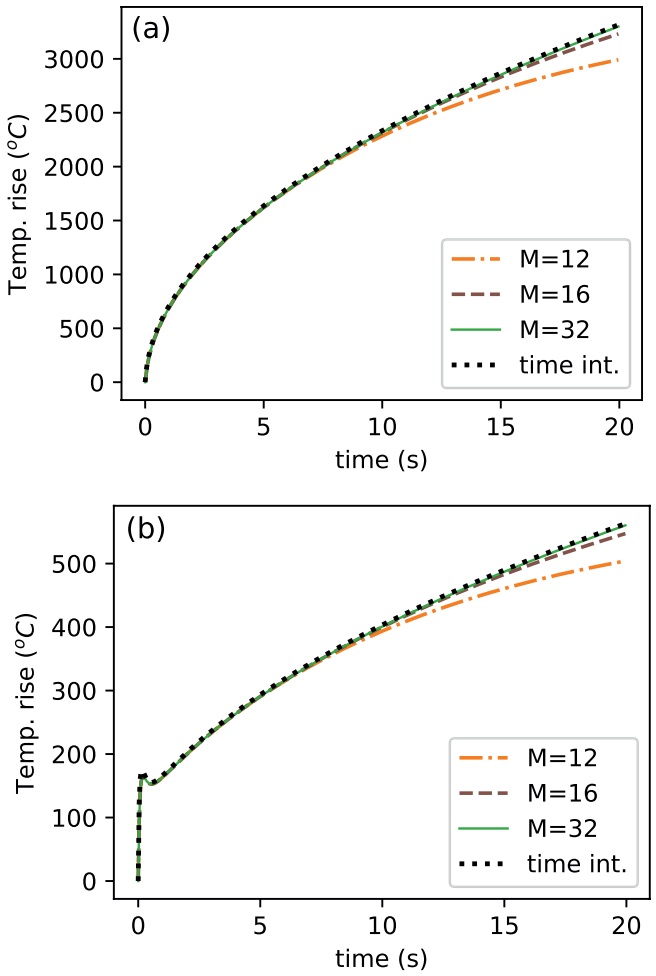

Figure A1. Test of the parsimonious scheme (wavenumber summation Equation A13). Temperature evolution is shown for (a) constant heat flux ($3\ 10^6 \mathrm{Wm}^{-2}$) and (b) exponentially decaying heat flux ($5\ 10^5 + 3\ 10^6 \exp(-10\ t)$). Solutions are shown for $M = 12, 16, 32$ (dot-dashed, dashed, and solid curve, respectively). For comparison, the solution obtained from the direct discretization (Equation A2) of the analytical solution (time integral) is shown (dotted curve). The time-stepping is $dt = 0.04$. See text for further details.

A3. In a Nutshell: The Temperature Update Scheme

Finally, we may sum-up the iterative scheme as follows. Upon discretization in time steps of size δt and M wavenumber steps of size δs, the memory variables θ_m are updated at each time iteration n, and summed in order to obtain the current temperature T according to:

$$\begin{aligned} \theta_m &= \left(\frac{q(n)\,\delta t}{\rho\, c} + \theta_m^- \right) \frac{1}{1 + \delta t\ \kappa\ s_m^2} \\ T(n) &= \frac{2}{\pi} \sum_{m=1}^{M} \theta_m\ \delta s \end{aligned} \tag{A13}$$

where θ_m^- is the m_{th} memory variable from the previous time step and s_m is defined in Equation A10. The above temperature T can then be used to update the temperature-dependent stress according to Equation 13. If the gradient of the temperature is required it can simply be obtained by

$$\partial_z T(t) = \frac{2}{\pi} \sum_{m=1}^{M} s_m\ \theta_m\ \delta s \tag{A14}$$

and temperature at a distance z from the source (fault plane) is obtained simply by:

$$T(z,t) = \frac{2}{\pi} \sum_{m=1}^{M} \cos(z\, s_m)\, \theta_m\, \delta s \tag{A15}$$

An adequate choice of s sampling is critical to achieve a good solution with a minimum number M of discrete wavenumbers s (and memory variables θ). Let's assume that the duration of interest is t_c and that we wish to obtain an approximate solution based on M wavenumbers. An indicative penetration depth for diffusion problems is $z_{max} \approx D\sqrt{\kappa\, t_c}$, where D is a dimensionless constant. We can use this formula to estimate a maximum wavelength in the problem, and we found that a good rule of thumb is $D = (2/5)M$. This rule may appear counter-intuitive, because the consequence of increasing M is to improve the sampling at small wavenumbers (long wavelengths) rather than at large wavenumbers. However, the larger error in this method is found at later times and larger scales. Therefore, extending the sampling toward low wavenumbers provides the maximum improvement. The minimum wavenumber is fixed by $s_{min} = 2\pi\ /\ z_{max} = 5\,\pi\ /\ (M\sqrt{\kappa\, t_c})$.

The minimum wavelength in the problem will be determined by the number of wavenumbers M such that $z_{\min} = z_{\max}/(2\,M)$ (i.e., in the center of the first wavelength interval). As a consequence, the maximum wavenumber is fixed by $s_{max} = 2\pi\ /\ z_{min} = 10\,\pi\ /\ \sqrt{\kappa\, t_c}$.

The wavenumber sampling step is $\delta s = s_{max}\ /\ M = 10\pi\ /\ (M\sqrt{\kappa\, t_c})$, and the sampling will take the form $s = (m - 1/2)\delta s$, $1 < m < M$.

For a practical example, let us use $t_c = 20$ s, $\kappa = 1.1\ 10^{-6}\mathrm{m^2 s^{-1}}$, $\rho = 3{,}000$, $c = 715$ $\delta t = 0.04$, $N = 500$. The discrete wavenumber solution is derived using $\delta s = 10\pi\ /\ (M\sqrt{\kappa\, t}) = 209.3\mathrm{radm^{-1}}$, and the sample wavenumbers are $s_m = (m - 1/2)\ \delta s$, where$(1 < m < M)$, which results in $s_m = (104.7, 313.96, 523.27, ...)$. In Figure A1, we show the results for three different samplings, $M = 12$, $M = 16$ and $M = 32$. For reference, we also show the result of time summation (Equation A2), which is a direct discretization of the analytical solution A1. Solutions are derived for either a constant heat flux ($q = 3$ MJ $\mathrm{m^{-2} s^{-1}}$) or an exponential decay ($q = 0.5 + 3$ $\exp(-t/0.1)$ MJ $\mathrm{m^{-2} s^{-1}}$).

For most practical purposes, $M = 16$ yields a satisfying approximation (with a precision of a few percent after $t = 20$s). $M = 32$ yields a result which differs less than 1/10,000 at $t = 20$ s when compared to the classic solution obtained by direct discretization (2). Timing the computation example above with $M = 16$ (on a desktop computer with python) yields 8.44 ms for the wavenumber solution versus 132 ms for the classic time summation, and storage of 16 floating point values versus 500, that is, an estimated gain of 97% in CPU time and 94% in memory storage.

A4. Finite Differences

The third type of temperature diffusion was tested, a finite differences Crank–Nicolson algorithm. The latter is the most flexible type of computation as it allows to consider parameters which are inhomogeneous along z and also variable in time (see Section 6 on thermal-dependent diffusivity and heat capacity).

Additional tests were performed using Fortran for the three types of the computation above, and using sufficient grid points in the finite difference scheme to avoid reflections from the end boundary of the grid. A sufficient precision was used for all 3 methods to diverge by no more than 2%. The resulting timing was: (1) wave number summation CPU time: 8.66E−2 s. Classic time summation CPU time: 0.30 s. Finite differences Crank–Nicolson CPU time: 1.87E−2 s.

Time summation is by far the less effective method in terms of time and memory usage, although it is easy to implement. The performance in time is of the same order for the wavenumber summation and the finite differences (in this example, the finite difference code is even more performant than the wavenumber summation).

Therefore, it is worth conducting the temperature solution using finite differences, for both best performance and increased flexibility. For the finite difference to work correctly, a sufficiently small spatial step should be selected (in our example, we use 2E−4 m) and in time (in our example, we use 10E−2 s) to

reflect the fastest changes expected in the heat flow regime. Once the duration of the simulation and the spatial step are determined, a sufficient number of nodes should be introduced to avoid reflections from the end boundary of the model (we use 50 nodes in this examples). To design the optimal parametrization, tests can be performed under the typical conditions required, decreasing the step size until reasonable convergence is achieved and increasing the number of steps until spurious boundary effects are negligible. In case that the thermal computation is coupled with a rupture model, the time steps in both methods need to be harmonized.

The above tests were performed on 16 CPUs Intel(R) Xeon(R) E5-2640 v3 clocked at 2.6 GHz. Example codes for temperature computation are provided in Supplementary Materials.

Appendix B: Temperature Evolution in the Presence of Melt Boundary Migration (Stefan Problem)

We consider the wavenumber solution in the case where a convection term is present, for example, due to the shortening of the sample occurring due to melting boundary migration combined with the extrusion of the melt (see Stefan problem solution in Nielsen et al., 2008; Nielsen, Di Toro, & Griffith, 2010). Assume that the boundary is migrating into the solid at a velocity v in direction z, and that in our referential z is attached to the boundary. In such case, the heat diffusion equation may be written with an additional term accounting for mass transport at velocity v equal and opposite to the boundary migration velocity:

$$\partial_t T = \kappa\, \partial_z^2 T + v\, \partial_z T + \frac{\delta(z)\, q}{\rho\, c}, \tag{B1}$$

which, in the wavenumber domain yields:

$$\partial_t \theta = -(\kappa\, s^2 + v\, s)\, \theta + \frac{q}{\rho\, c}. \tag{B2}$$

(Note that here z is the distance from the melting boundary, in the Eulerian referential not attached to the flow of particles.) The only difference with the previous solution is the replacement $\kappa\, s \rightarrow (\kappa\, s^2 + v\, s)$ so that we may write

$$T(z=0,t) = \frac{2}{\pi\rho\, c}\int_0^t dt' \int_0^\infty ds\; q(t')\, e^{-(\kappa\, s^2 + v\, s)(t-t')} \tag{B3}$$

and solving for the inner integral we obtain

$$T = \frac{1}{\rho\, c\, \sqrt{\pi\kappa}}\int_0^t dt' \frac{q(t')}{\sqrt{t-t'}}\, f_a(t-t') \tag{B4}$$

where

$$f_a(t) = e^{\frac{v^2 t}{4\kappa}}\, \mathrm{Erfc}\left(v(t)\sqrt{\frac{t}{4\,\kappa}}\right) \tag{B5}$$

Interestingly, we remark that the solution is in all points similar to the previous, except for the multiplication by function $f_a(t)$ which behaves essentially like a memory-fading term with a characteristic time of about $t_c = 4\kappa/v^2$ (making the approximation that $v \approx$ Const. Quite intuitively, t_c is the average time of residence of heat inside the solid before it is erased by the shortening process. Indeed, if we write the penetration depth for diffusion during an interval t_c as $z = 2\sqrt{\kappa\, t_c}$, and we write the advancement of the boundary as $z = v\, t_c$, if we equate both values of z we obtain the same value for t_c.

There are ways to obtain a numerical solution of the wavenumber formulation (Equation B2) in the presence of a migrating boundary. We do not see the necessity to develop this here, because the finite difference method is equally efficient and capable of handling the migrating boundary (Nielsen, Mosca, et al., 2010).

Appendix C: Analytical Solution of Equation A4

Multiplying by a dummy function u, we may write

$$\partial_t(u\,\theta) - \theta\,\partial_t u = -u\,\kappa\,s^2\theta + u\,\frac{q}{\rho\,c} \tag{C1}$$

and assume the arbitrary function u is such that both following parts of the equation are zero:

$$(u\,\kappa\,s^2 - \partial_t u)\,\theta \;=\; 0 \tag{C2}$$

$$\partial_t(u\,\theta) - u\,\frac{q}{\rho\,c} \;=\; 0 \tag{C3}$$

excluding the trivial solution $\theta = 0$, the first equation yields

$$u = A\,\exp\{\kappa s^2 t\} \tag{C4}$$

replacing u into the second equation and integrating in time we obtain

$$\theta = \frac{1}{\rho\,c}\,e^{-\kappa s^2 t}\int_0^t q(t')\,e^{\kappa s^2 t'}\,dt' \tag{C5}$$

$$\theta = \frac{1}{\rho\,c}\int_0^t q(t')\,e^{-\kappa s^2 (t-t')}\,dt' \tag{C6}$$

(an extra integration constant vanishes since temperature is zero at negative times). The solution for $T(x, t)$ is obtained by performing the inverse Cosine transform

$$T(x,t) = \frac{2}{\pi}\int_0^\infty \mathrm{Cos}(s\,z)\,\theta(s,t)\,ds \tag{C7}$$

and, at $z = 0$,

$$T(0,t) = \frac{2}{\pi}\int_0^\infty \theta(s,t)\,ds. \tag{C8}$$

Upon replacement of θ by its expression, we get

$$= \frac{2}{\pi\rho\,c}\int_0^\infty \mathrm{Cos}(s\,z)\left(\int_0^t q(t')\,e^{-\kappa s^2 (t-t')}\,dt'\right)ds \tag{C9}$$

$$= \frac{2}{\pi\rho\,c}\int_0^t dt'\int_0^\infty ds\,\mathrm{Cos}(s\,z)\,q(t')\,e^{-\kappa s^2 (t-t')} \tag{C10}$$

By integrating the inner part, we obtain

$$\frac{1}{\rho\, c\, \sqrt{\pi\kappa}} \int_0^t \frac{q(t')\, e^{-\frac{z^2}{4\kappa(t-\mathrm{tt})}}}{\sqrt{t-t'}}\, dt' \tag{C11}$$

where we can check for consistency that we retrieve the classical solution of Equation 2 by setting $z = 0$.

Appendix D: Regularization for Use in Dynamic Rupture Modeling

In dynamic rupture models, the slip velocity history is a result of the computation; it is not imposed and not known a priori. Thus, the frictional form Equation 13 with its strong rate dependence may generate very abrupt and fast weakening, resulting in under-sampling of the rupture front by the numerical scheme, and the consequent artifacts in the results. A similar situation arises in the ill-posed problem of rupture at bi-material interfaces, where a contracting slip pulse rapidly becomes under-sampled (Andrews & Ben-Zion, 1997).

This problem can be circumvented by introducing a regularized shear stress value τ_{reg} which obeys a time-dependent evolution law. Let τ be the target value of shear stress at time t, which is obtained by implementing a law (such as flash weakening described in Section 5). We can write a regularized form of shear stress τ_{reg} by adding a time-evolution law on top of the instantaneous value of friction such that

$$\frac{\partial \tau_{\mathrm{reg}}}{\partial t} = \frac{\tau - \tau_{\mathrm{reg}}}{t_a} \tag{D1}$$

which by the usual first-order backward Euler scheme result in the discrete form

$$\tau_{reg} = \frac{\bar{\tau_{reg}} + \frac{\delta t}{t_a}\tau}{1 + \frac{\delta t}{t_a}} \tag{D2}$$

where $\bar{\tau_{reg}}$ is the value at the previous time step.

Thus, t_a can be fixed to the lowest limit compatible with the numerical grid, producing a regularized (smoothed) solution. In principle, with sufficient computing resources the numerical grid spacing and t_a may be reduced until τ and τ_{reg} converge.

Data Availability Statement

The data used in this article are available at the following public repository: https://datahub.io/stefanazzz/thermal-weakening-2021/v/1.

Acknowledgments
The authors acknowledge the support by ERC CoG No. 6145705 NOFEAR. The authors thank the anonymous reviewer for suggesting that we illustrate the effects of thermal dependence of diffusivity and capacity, and Alice Gabriel for suggesting that we include the finite difference method in the efficiency tests.

References

Acosta, M., Passelègue, F. X., Schubnel, A., & Violay, M. (2018). Dynamic weakening during earthquakes controlled by fluid thermodynamics. *Nature Communications*, *9*, 3074. https://doi.org/10.1038/s41467-018-05603-9

Andrews, D. J., & Ben-Zion, Y. (1997). Wrinkle-like slip pulse on a fault between different materials. *Journal of Geophysical Research*, *102*, 552–571. https://doi.org/10.1029/96jb02856

Archard, J. F. (1959). The temperature of rubbing surfaces. *Wear*, *2*(6), 438–455. https://doi.org/10.1016/0043-1648(59)90159-0

Atkins, A. G., & Tabor, D. (1965). Plastic indentation in metals with cones. *Journal of the Mechanics and Physics of Solids*, *13*(3), 149–164. https://doi.org/10.1016/0022-5096(65)90018-9

Beeler, N. M., Tullis, T. E., & Goldsby, D. L. (2008). Constitutive relationships and physical basis of fault strength due to flash heating. *Journal of Geophysical Research*, *113*(B1), B01401. https://doi.org/10.1029/2007JB004988

Brantut, N., Han, R., Shimamoto, T., Findling, N., & Schubnel, A. (2010). Fast slip with inhibited temperature rise due to mineral dehydration: Evidence from experiments on gypsum. *Geology*, *39*(1), 59–62. https://doi.org/10.1130/g31424.1

Brantut, N., & Platt, J. D. (2017). Dynamic weakening and the depth dependence of earthquake faulting. In *Fault zone dynamic processes* (pp. 171–194). American Geophysical Union (AGU). https://doi.org/10.1002/9781119156895.ch9

Brantut, N., & Viesca, R. C. (2017). The fracture energy of ruptures driven by flash heating. *Geophysical Research Letters*, *44*(13), 6718–6725. https://doi.org/10.1002/2017GL074110
Carslaw, H. S., & Jaeger, J. C. (1959). *Conduction of heat in solids*. Oxford University Press.
Chang, J. C., Lockner, D. A., & Reches, Z. (2012). Rapid acceleration leads to rapid weakening in earthquake-like laboratory experiments. *Science*, *338*(6103), 101–105. https://doi.org/10.1126/science.1221195
Chen, J., & Rempel, A. W. (2014). Progressive flash heating and the evolution of high-velocity rock friction. *Journal of Geophysical Research: Solid Earth*, *119*(4), 3182–3200. https://doi.org/10.1002/2013jb010631
Collettini, C., Niemeijer, A., Viti, C., Smith, S. A. F., & Marone, C. (2011). Fault structure, frictional properties and mixed-mode fault slip behavior. *Earth and Planetary Science Letters*, *311*(3–4), 316–327. https://doi.org/10.1016/j.epsl.2011.09.020
Cornelio, C., Passelègue, F. X., Spagnuolo, E., Di Toro, G., & Violay, M. (2020). Effect of fluid viscosity on fault reactivation and coseismic weakening. *Journal of Geophysical Research: Solid Earth*, *125*(1), e2019JB018883. https://doi.org/10.1029/2019JB018883
Cornelio, C., Spagnuolo, E., Di Toro, G., Nielsen, S., & Violay, M. (2019). Mechanical behavior of fluid-lubricated faults. *Nature Communications*, *10*, 1274. https://doi.org/10.1038/s41467-019-09293-9
Cruz-Atienza, V. M., & Olsen, K. B. (2010). Supershear mach-waves expose the fault breakdown slip. *Tectonophysics*, *493*, 285–296. https://doi.org/10.1016/j.tecto.2010.05.012,2010
De Paola, N., Collettini, C., Faulkner, D. R., & Trippetta, F. (2008). Fault zone architecture and deformation processes within evaporitic rocks in the upper crust. *Tectonics*, *27*(4), TC4017. https://doi.org/10.1029/2007tc002230
Dieterich, J. H. (1979). Modeling of rock friction: 1. Experimental results and constitutive equations. *Journal of Geophysical Research*, *84*, 2161–2168. https://doi.org/10.1029/jb084ib05p02161
Di Toro, G., Goldsby, D. L., & Tullis, T. E. (2004). Friction falls toward zero in quartz rock as slip velocity approaches seismic rates. *Nature*, *427*, 436–439. https://doi.org/10.1038/nature02249
Di Toro, G., Han, R., Hirose, T., De Paola, N., Nielsen, S., Mizoguchi, K., et al. (2011). Fault lubrication during earthquakes. *Nature*, *471*, 494–498. https://doi.org/10.1038/nature09838
Di Toro, G., Hirose, T., Nielsen, S., Pennacchioni, G., & Shimamoto, T. (2006). Natural and experimental evidence of melt lubrication of faults during earthquakes. *Science*, *311*, 647–649. https://doi.org/10.1126/science.1121012
Di Toro, G., Nielsen, S., & Pennacchioni, G. (2005). Earthquake rupture dynamics frozen in exhumed ancient faults. *Nature*, *436*, 1009–1012. https://doi.org/10.1038/nature03910
Fondriest, M., Smith, S. A. F., Candela, T., Nielsen, S. B., Mair, K., & Di Toro, G. (2013). Mirror-like faults and power dissipation during earthquakes. *Geology*, *41*(11), 1175–1178. https://doi.org/10.1130/G34641.1
Fulton, P. M., Brodsky, E. E., Kano, Y., Mori, J., Chester, F., Ishikawa, T., et al. (2013). Low coseismic friction on the Tohoku-Oki fault determined from temperature measurements. *Science*, *342*(6163), 1214–1217. https://doi.org/10.1126/science.1243641
Goldsby, D. L., & Tullis, T. E. (2011). Flash heating leads to low frictional strength of crustal rocks at earthquake slip rates. *Science*, *334*(6053), 216–218. https://doi.org/10.1126/science.1207902
Han, R., Shimamoto, T., Hirose, T., Ree, J.-H., & Ando, J.-i. (2007). Ultralow friction of carbonate faults caused by thermal decomposition. *Science*, *316*, 878–881. https://doi.org/10.1126/science.1139763
Hardebeck, J. L. (2015). Stress orientations in subduction zones and the strength of subduction megathrust faults. *Science*, *349*(6253), 1213–1216. https://doi.org/10.1126/science.aac5625
Hasegawa, A., Yoshida, K., & Okada, T. (2011). Nearly complete stress drop in the 2011 m w 9.0 off the pacific coast of Tohoku earthquake. *Earth, Planets and Space*, *63*(7), 703–707. https://doi.org/10.5047/eps.2011.06.007
Hirose, T., & Shimamoto, T. (2005). Growth of molten zone as a mechanism of slip weakening of simulated faults in gabbro during frictional melting. *Journal of Geophysical Research*, *110*, B05202. https://doi.org/10.1029/2004JB003207
Hirth, G., & Beeler, N. M. (2015). The role of fluid pressure on frictional behavior at the base of the seismogenic zone. *Geology*, *43*(3), 223–226. https://doi.org/10.1130/G36361.1
Hirth, G., & Kohlstedt, D. (2004). Inside the subduction factory. In J. Eiler (Ed.), *Rheology of the upper mantle and the mantle wedge: A view from the experimentalists*. American Geophysical Union. https://doi.org/10.1029/138GM06
Hung, C. C., Kuo, L. W., Spagnuolo, E., Wang, C. C., Di Toro, G., Wu, W. J., et al. (2019). Grain fragmentation and frictional melting during initial experimental deformation and implications for seismic slip at shallow depths. *Journal of Geophysical Research: Solid Earth*, *124*(11), 11150–11169. https://doi.org/10.1029/2019JB017905
Kaneko, Y., Fukuyama, E., & Hamling, I. J. (2017). Slip-weakening distance and energy budget inferred from near-fault ground deformation during the 2016 Mw7.8 Kaikōura earthquake. *Geophysical Research Letters*, *44*(10), 4765–4773. https://doi.org/10.1002/2017gl073681. https://doi.org/10.1002/2017GL073681
Karato, S.-I. (2008). *Deformation of earth materials: An introduction to the rheology of solid earth*. Cambridge University Press.
King, D. S. H., & Marone, C. (2012). Frictional properties of olivine at high temperature with applications to the strength and dynamics of the oceanic lithosphere. *Journal of Geophysical Research*, *117*(117), B12203. https://doi.org/10.1029/2012jb009511
Lankford, J. (1996). High strain rate compression and plastic flow of ceramics. *Journal of Materials Science Letters*, *15*, 445–450. https://doi.org/10.1007/bf00274593
Marone, C. (1998). Laboratory-derived friction laws and their application to seismic faulting. *Annual Review of Earth and Planetary Sciences*, *26*, 643–696. https://doi.org/10.1146/annurev.earth.26.1.643
Merriman, J. D., Hofmeister, A. M., Roy, D. J., & Whittington, A. G. (2018). Temperature-dependent thermal transport properties of carbonate minerals and rocks. *Geosphere*, *14*(4), 1961–1987. https://doi.org/10.1130/ges01581.1
Miao, S. Q., Li, H. P., & Chen, G. (2014). Temperature dependence of thermal diffusivity, specific heat capacity, and thermal conductivity for several types of rocks. *Journal of Thermal Analysis and Calorimetry*, *115*(2), 1057–1063. https://doi.org/10.1007/s10973-013-3427-2
Mitchell, T. M., Smith, S. A. F., Anders, M. H., Di Toro, G., Nielsen, S., Cavallo, A., & Beard, A. D. (2015). Catastrophic emplacement of giant landslides aided by thermal decomposition: Heart Mountain, Wyoming. *Earth and Planetary Science Letters*, *411*, 199–207. https://doi.org/10.1016/j.epsl.2014.10.051
Mizoguchi, K., Hirose, T., Shimamoto, T., & Fukuyama, E. (2007). Reconstruction of seismic faulting by high-velocity friction experiments: An example of the 1995 Kobe earthquake. *Geophysical Research Letters*, *34*, L01308. https://doi.org/10.1029/2006GL027931
Nielsen, S., Di Toro, G., Hirose, T., & Shimamoto, T. (2008). Frictional melt and seismic slip. *Journal of Geophysical Research*, *113*, B01308. https://doi.org/10.1029/2007JB005122
Nielsen, S., & Madariaga, R. (2003). On the self-healing fracture mode. *Bulletin of the Seismological Society of America*, *93*(6), 2375–2388. https://doi.org/10.1785/0120020090

Nielsen, S., Mosca, P., Giberti, G., Di Toro, G., Hirose, T., & Shimamoto, T. (2010). On the transient behavior of frictional melt during seismic slip. *Journal of Geophysical Research*, *115*, B10301. https://doi.org/10.1029/2009JB007020

Nielsen, S., Spagnuolo, E., Smith, S. A. F., Violay, M., Di Toro, G., & Bistacchi, A. (2016). Scaling in natural and laboratory earthquakes. *Geophysical Research Letters*, *43*(4), 1504–1510. https://doi.org/10.1002/2015GL067490

Nielsen, S., Spagnuolo, E., Violay, M., Smith, S., Di Toro, G., & Bistacchi, A. (2016). G: Fracture energy, friction and dissipation in earthquakes. *Journal of Seismology*, *20*, 1–19. https://doi.org/10.1007/s10950-016-9560-1

Nielsen, S., Di Toro, G. D., & Griffith, W. A. (2010). Friction and roughness of a melting rock surface. *Geophysical Journal International*, *182*, 299–310. https://doi.org/10.1111/j.1365-246X.2010.04607.x

Niemeijer, A., Di Toro, G., Nielsen, S., Smith, S., Griffith, W. A., Scarlato, P., et al. (2009). A new state-of-the-art tool to investigate rock friction under extreme slip velocities and accelerations: Shiva. In *Eos, Transactions American Geophysical Union (Fall Meet. Suppl.)* (Abs. T23C-1950) (Vol. 90 (52))

Noda, H., Dunham, E. M., & Rice, J. R. (2009). Earthquake ruptures with thermal weakening and the operation of major faults at low overall stress levels. *Journal of Geophysical Research*, *114*, B07302. https://doi.org/10.1029/2008JB006143

Noda, H., Kanagawa, K., Hirose, T., & Inoue, A. (2011). Frictional experiments of dolerite at intermediate slip rates with controlled temperature: Rate weakening or temperature weakening?. *Journal of Geophysical Research*, *116*(B7), B07306. https://doi.org/10.1029/2010JB007945

Noda, H., & Lapusta, N. (2010). Three-dimensional earthquake sequence simulations with evolving temperature and pore pressure due to shear heating: Effect of heterogeneous hydraulic diffusivity. *Journal of Geophysical Research*, *115*(B12). https://doi.org/10.1029/2010JB007780

Otsuki, K., Monzawa, N., & Nagase, T. (2003). Fluidization and melting of fault gouge during seismic slip: Identification in the Nojima fault zone and implications for focal earthquake mechanisms. *Journal of Geophysical Research*, *108*(B4). https://doi.org/10.1029/2001JB001711

Passelègue, F. X., Goldsby, D. L., & Fabbri, O. (2014). The influence of ambient fault temperature on flash-heating phenomena. *Geophysical Research Letters*, *41*(3), 828–835. https://doi.org/10.1002/2013GL058374

Persson, B. N. J. (2000). *Sliding friction, physical principles and applications*. In K. von Klitzing, & R. Wiesendanger (Eds.). Springer-Verlag.

Poirier, J.-P. (1985). *Creep of crystals: High-temperature deformation processes in metals, ceramics and minerals*. Cambridge University Press.

Pozzi, G., De Paola, N., Holdsworth, R. E., Bowen, L., Nielsen, S. B., & Dempsey, E. D. (2019). Coseismic ultramylonites: An investigation of nanoscale viscous flow and fault weakening during seismic slip. *Earth and Planetary Science Letters*, *516*, 164–175. https://doi.org/10.1016/j.epsl.2019.03.042

Pozzi, G., De Paola, N., Nielsen, S. B., Holdsworth, R. E., & Bowen, L. (2018). A new interpretation for the nature and significance of mirror-like surfaces in experimental carbonate-hosted seismic faults. *Geology*, *46*(7), 583–586. https://doi.org/10.1130/g40197.1

Proctor, B. P. T. M., Mitchell, T, Goldsby, D., Zorzi, F., Platt, J. D., et al. (2014). Dynamic weakening of serpentinite gouges and bare surfaces at seismic slip rates. *Journal of Geophysical Research: Solid Earth*, *119*, 8107. https://doi.org/10.1002/2014JB011057

Raterron, P., Wu, Y., Weidner, D. J., & Chen, J. (2004). Low-temperature olivine rheology at high pressure. *Physics of the Earth and Planetary Interiors*, *145*(1), 149–159. https://doi.org/10.1016/j.pepi.2004.03.007

Rempel, A. W., & Rice, J. R. (2006). Thermal pressurization and onset of melting in fault zones. *Journal of Geophysical Research*, *111*, B09314. https://doi.org/10.1029/2006JB004314

Rempel, A. W., & Weaver, S. L. (2008). A model for flash weakening by asperity melting during high-speed earthquake slip. *Journal of Geophysical Research*, *113*(B11), B11308. https://doi.org/10.1029/2008JB005649

Rice, J. (1999). Flash heating at asperity contacts and rate-dependent friction. *Eos, Transactions American Geophysical Union*, *80*(46), F681l.

Rice, J. R. (2006). Heating and weakening of faults during earthquake slip. *Journal of Geophysical Research*, *111*. https://doi.org/10.1029/2005JB004006

Richter, D., & Simmons, G. (1974). Thermal expansion behavior of igneous rocks. In *International Journal of Rock Mechanics and Mining Sciences & Geomechanics* Abstracts (Vol. 11, No. 10, pp. 403-411). Pergamon.

Ruina, A. (1983). Slip instability and state variable friction laws. *Journal of Geophysical Research*, *88*, 10359–10370. https://doi.org/10.1029/jb088ib12p10359

Sibson, R. H. (2003). Thickness of the seismic slip zone. *Bulletin of the Seismological Society of America*, *93*(3), 1169–1178. https://doi.org/10.1785/0120020061

Smith, S. A. F., Nielsen, S., & Di Toro, G. (2015). Strain localization and the onset of dynamic weakening in calcite fault gouge. *Earth and Planetary Science Letters*, *413*, 25–36. https://doi.org/10.1016/j.epsl.2014.12.043

Sone, H., & Shimamoto, T. (2009). Frictional resistance of faults during accelerating and decelerating earthquake slip. *Nature Geoscience*, *2*, 705. https://doi.org/10.1038/NGEO637

Spudich, P. (1998). Use of fault striations and dislocation models to infer tectonic shear stress during the 1995 Hyogo-ken Nanbu (Kobe), Japan, earthquake. *Bulletin of the Seismological Society of America*, *88*, 413–427.

Sulem, J., Famin, V., & Noda, H. (2009). Correction to "Thermal decomposition of carbonates in fault zones: Slip-weakening and temperature-limiting effects". *Journal of Geophysical Research*, *114*, B03309. https://doi.org/10.1029/2008JB00600410.1029/2009jb006576

Tisato, N., Di Toro, G., De Rossi, N., Quaresimin, M., & Candela, T. (2012). Experimental investigation of flash weakening in limestone. *Journal of Structural Geology*, *38*, 183–199. https://doi.org/10.1016/j.jsg.2011.11.017

Tsutsumi, A., & Shimamoto, T. (1997). High-velocity frictional properties of gabbro. *Geophysical Research Letters*, *24*, 699–702. https://doi.org/10.1029/97gl00503

Ulrich, T., Gabriel, A.-A., Ampuero, J.-P., & Xu, W. (2019). Dynamic viability of the 2016 mw 7.8 kaiko¯ura earthquake cascade on weak crustal faults. *Nature Communications*, *10*(1), 1213.

Viesca, R. C., & Garagash, D. I. (2015). Ubiquitous weakening of faults due to thermal pressurization. *Nature Geoscience*, *8*, 875. https://doi.org/10.1038/ngeo2554

Violay, M., Di Toro, G., Gibert, B., Nielsen, S., Spagnuolo, E., Del Gaudio, P., et al. (2014). Effect of glass on the frictional behavior of basalts at seismic slip rates. *Geophysical Research Letters*, *41*(2), 348–355. https://doi.org/10.1002/2013gl058601

Violay, M., Di Toro, G., Nielsen, S., Spagnuolo, E., & Burg, J. P. (2015). Thermo-mechanical pressurization of experimental faults in cohesive rocks during seismic slip. *Earth and Planetary Science Letters*, *429*, 1–10. https://doi.org/10.1016/j.epsl.2015.07.054

Violay, M., Gibert, B., Mainprice, D., Evans, B., Dautria, J.-M., Azais, P., & Pezard, P. (2012). An experimental study of the brittle-ductile transition of basalt at oceanic crust pressure and temperature conditions. *Journal of Geophysical Research*, *117*(B3). https://doi.org/10.1029/2011JB008884

Violay, M., Nielsen, S., Cinti, D., Spagnuolo, E., Di Toro, G., & Smith, S. (2011). Friction of marble under seismic deformation conditions in the presence of fluid. In: *Agu 2011 fall meeting*.

Violay, M., Nielsen, S., Gibert, B., Spagnuolo, E., Cavallo, A., Azais, P., et al. (2013). Effect of water on the frictional behavior of cohesive rocks during earthquakes. *Geology*, *42*(1), 27–30. https://doi.org/10.1130/G34916.1

Violay, M., Nielsen, S., Spagnuolo, E., Cinti, D., Di Toro, G., & Di Stefano, G. (2013). Pore fluid in experimental calcite-bearing faults: Abrupt weakening and geochemical signature of co-seismic processes. *Earth and Planetary Science Letters*, *361*(0), 74–84. https://doi.org/10.1016/j.epsl.2012.11.021

Violay, M., Passelegue, F., Spagnuolo, E., Di Toro, G., & Cornelio, C. (2019). Effect of water and rock composition on re-strengthening of cohesive faults during the deceleration phase of seismic slip pulses. *Earth and Planetary Science Letters*, *522*, 55–64. https://doi.org/10.1016/j.epsl.2019.06.027

Weidner, D. J., Wang, Y., & Vaughan, M. T. (1994). Yield strength at high pressure and temperature. *Geophysical Research Letters*, *21*(9), 753–756. https://doi.org/10.1029/93gl03549

Yao, L., Ma, S., Platt, J. D., Niemeijer, A. R., & Shimamoto, T. (2016). The crucial role of temperature in high-velocity weakening of faults: Experiments on gouge using host blocks with different thermal conductivities. *Geology*, *44*(1), 63–66. https://doi.org/10.1130/G37310.1

Yuan, F., & Prakash, V. (2008). Slip weakening in rocks and analog materials at co-seismic slip rates. *Journal of the Mechanics and Physics of Solids*, *56*, 542–560. https://doi.org/10.1016/j.jmps.2007.05.007

Yuan, F., & Prakash, V. (2012). Laboratory observations of transient frictional slip in rock-analog materials at co-seismic slip rates and rapid changes in normal stress. *Tectonophysics*, *558–559*, 58–69. https://doi.org/10.1016/j.tecto.2012.06.026

Zheng, G., & Rice, J. (1998). Conditions under which velocity weakening friction allows a self-healing versus a cracklike mode of rupture. *Bulletin of the Seismological Society of America*, *88*(6), 1466–1483.